Scanning Microscopy

Volume 6 | Number 3 Article 2

4-2-1992

The Scanning Probe Microscope

J. Jahanmir
WYKO Corporation

B. G. Haggar
WYKO Corporation

J. B. Hayes
WYKO Corporation

Scanning Microscopy, Vol. 6, No. 3, 1992 (Pages 625-660) 0891-7035/92$5.00+.00
Scanning Microscopy International, Chicago (AMF O'Hare), IL 60666 USA

THE SCANNING PROBE MICROSCOPE

J. Jahanmir*, B.G. Haggar, and J.B. Hayes

WYKO Corporation, Tucson, AZ 85706

(Received for publication June 14, 1991, and in revised form April 2, 1992)

Abstract

Scanning probe microscopy has evolved into a powerful tool since its inception in 1982. The scanning probe microscope has found applications in metrology, spectroscopy, and lithography. We will review the background of the technology, discuss the different types of scanning probe microscopes including the scanning tunneling microscope and the scanning force microscope, and present many of the applications for the instrument.

Key Words: Microscopy; scanning probe microscopy; atomic force microscopy; scanning tunneling microscopy.

*Address for correspondence:
J. Jahanmir,
WYKO Corporation,
2650 E. Elvira Road,
Tucson, AZ 85706.

Tel.: (602) 741-1044
Fax: (602) 294-1799

Introduction

The scanning tunneling microscope (STM) was developed by Binnig and Rohrer (1982) in 1982. Since then, the STM has found numerous applications in science and technology. The STM's atomic resolution allows local characterization of surfaces. It is capable of measuring surface topography, electrical conductivity, electronic structure, and atomic structure.

The scanning tunneling microscope is based on the principle of quantum mechanical tunneling of electrons between two electrodes under an applied electric field. One of the electrodes, the sample, is usually stationary while the other, an atomically sharp metal tip, is scanned over the sample. The tip is mounted on piezoelectric ceramic materials and is capable of moving in the x, y, and z directions by the application of electric fields to the piezoelectric ceramics (Figure 1).

In one mode of operation, a potential is applied to the z-ceramic through a feedback control unit, maintaining constant tip-to-sample current. Operated in this manner, the tip moves in the x, y, and z directions, following the topography of the surface. The lateral resolution of the STM is determined by the tip geometry. By using proper tip preparation techniques, spatial resolution on the order of 1 Å or less can be obtained.

Young *et al.* (1972) were the first research group to use a similar non-contacting instrument, the Topografiner, to measure the microtopography of metallic surfaces. They were able to obtain low resolution images by operating the tip in the field emission mode with tip-to-sample spacings on the order of 200 Å. They also demonstrated the linear dependence of the tunneling current between the tip and the sample on the applied voltage for small vacuum gaps and low voltages. The lack of sufficient vibration isolation prevented them from imaging in the tunneling mode.

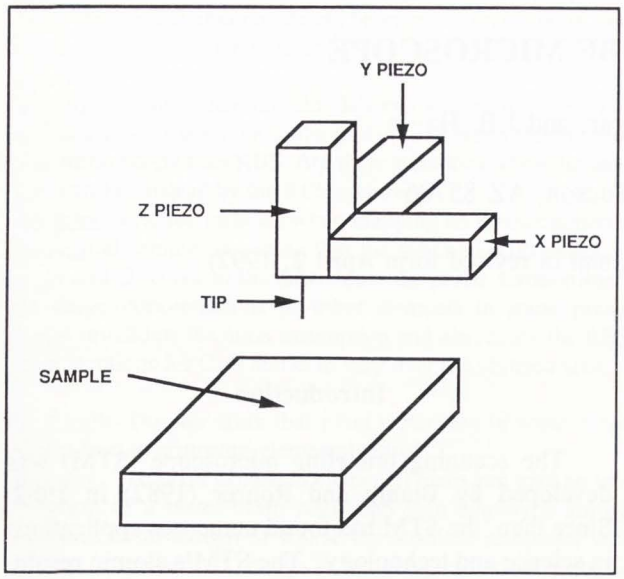

Figure 1. Schematic of the tip scanning geometry, depicting the x, y, and z direction piezoelectric ceramics.

Using an approach similar to Young *et al.* (1972) but with a more elaborate vibration isolation system, Binnig and Rohrer (1982) were able to obtain images of atomic steps on Au(110), Si(111), and GaAs(111). In a further development, they reported the first images of the 7x7 reconstruction of Si(111), with atomic resolution in real space (Binnig *et al.*, 1983a). This was followed by the atomic resolution studies of reconstructions of Au(110) (Binnig *et al.*, 1983b) and Au(100) (Binnig *et al.*, 1984) surfaces.

Since then, the STM has evolved into a powerful tool for spectroscopy, metrology, and nanolithography. Many other instruments have also evolved from the STM technology. Among those instruments, the scanning force microscope (SFM) is one of the most important ones. In this paper we will review the STM and SFM technologies and their many applications. In the "Theoretical" section we will review the basic theory of the STM and discuss the resolution of the instrument. In the "Experimental" section we will cover the basic mechanical and electronic design and vibration isolation requirements for the STM. In that section we will also present probe tip preparation methods and discuss the effects of tip geometry on image quality and resolution. In the "Applications" section, we will discuss the applications of the STM to atomic orientation on surfaces, spectroscopy, electrochemistry, nanofabrication, biological materials, and topography. In the "Scanning Force Microscope" section, the SFM is discussed. The "Applications of SFM" section covers the applications of SFM to the study of tip-sample interactions such as friction, van der Waals, magnetic, and electrostatic forces. Also, SFM capabilities for imaging magnetic domains, surface structure, and biological materials are discussed. In the "Related Techniques" section, other techniques that are based on STM technology are presented.

Theoretical

Tunneling current depends on the overlap of the wave functions of the tip and the sample. Under normal tunneling conditions the interaction between the tip and the sample is weak and first order perturbation theory can be used (Tersoff and Hamann, 1983):

$$J = \frac{2\pi e}{\hbar} \sum_{\mu\ \nu} f(E_\mu)[1-f(E_\nu+eV)]\,|M_{\mu\nu}|^2\,\delta(E_\mu-E_\nu) \quad (1)$$

where $M_{\mu\nu}$ is the tunneling matrix and f(E) and f(E+eV) are the Fermi-Dirac occupation factors at the energies E and E+eV of the two electrodes. Using Bardeen's formulation, M is given by (Bardeen, 1961):

$$M_{\mu\nu} = \frac{\hbar^2}{2m}\int dS\cdot(\psi_\mu^* \nabla \psi_\nu - \psi_\nu \nabla \psi_\mu^*) \quad (2)$$

where ψ_μ and ψ_ν are the wave functions. The general three-dimensional analysis of the above equations is quite complicated and is beyond the scope of this review. The wave functions for the one-dimensional case are given by (Feenstra, 1990):

$$\psi_\mu = \overset{\circ}{\psi}_\mu \exp(-z)$$

and (3)

$$\psi_\nu = \overset{\circ}{\psi}_\nu \exp[-\kappa(s-z)]$$

where

$$\kappa = \sqrt{\frac{2m\phi}{\hbar^2}}$$

s is the spacing between the two electrodes, z is the integration parameter, κ is the decay constant of the wave functions and ϕ is the work function, which is assumed to be the same for both electrodes. Substituting into equations (2) and (1), we find:

we find:

$$I \propto \sum_{\mu} \sum_{\nu} |\psi^{\circ}_{\mu}|^2 \, |\psi^{\circ}_{\nu}|^2 \exp(-2\kappa s).$$

The current depends exponentially on the tip-to-sample spacing. For a work function of 4 eV, $\kappa = 1.0$ Å^{-1}. When the gap spacing is changed by 1 Å, the current changes by a factor of 10. For a 0.1 Å vertical resolution, the tip-to-sample current has to remain constant by 20%.

The lateral resolution for imaging purposes with low applied voltages ($<< 1$V) has been formulated for a surface with a weak sinusoidal corrugation with amplitude $h_s/2$ by Stoll (1984):

$$\frac{\Delta d}{h_s} = \exp\left\{\frac{-\pi^2(s+r_t)}{\kappa a^2}\right\}$$

where $\Delta d/2$ is the amplitude of the observed corrugation of the equicurrent surface, s is the tip-to-sample spacing, r_t is the tip radius, a is the corrugation period, and κ is the decay constant of the wave functions given above.

Experimental

Mechanical System

The design criterion for STM is that the tip-to-sample position control should be better than the resolution desired. For atomic resolution imaging, the tip position has to be resolved 0.1 Å vertically and 1 Å laterally. The dynamic range required for atomic resolution imaging is a few thousand Ångstroms in the x, y and z directions. An approach mechanism is also required for coarse and fine positioning of the probe tip on the sample.

The scanning requirements are satisfied by the use of piezoelectric ceramics. Piezoelectric ceramics are capable of position control down to 0.01 Å or better, with a dynamic range of several μm. The piezoelectric ceramics can be mounted in an orthogonal tripod arrangement for scanning in x, y and z such as shown in Figure 1. This design is mechanically subject to low resonance frequencies. An implementation developed by Binnig and Smith (1986) uses a single tube ceramic for scanning the probe tip. The outer electrode of the tube is sectioned into four equal parts parallel to the axis of the tube (see Figure 2). Scanning is performed by applying voltages V_x and $-V_x$ to two opposing electrodes and V_y and $-V_y$ to the remaining two. The voltage applied to the inner electrode is used for motion in the z direction.

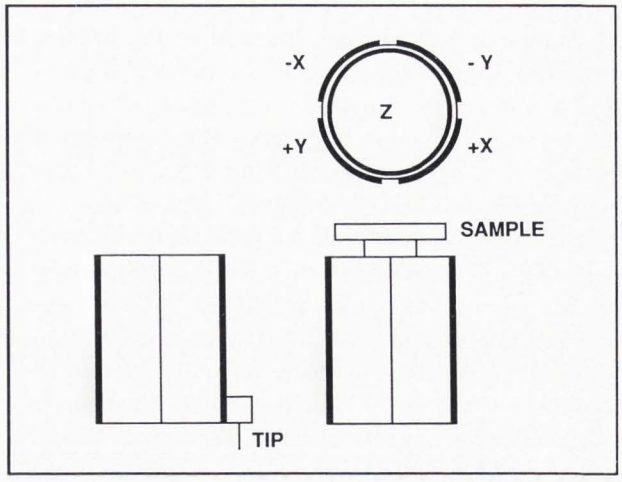

Figure 2. Schematic representation of a tube ceramic used for scanning in the x, y, and z directions. The outer electrode of the tube ceramic is sectioned into four equal parts parallel to the axis of the tube. Scanning is performed by applying voltages V_x and $-V_x$ to two opposing electrodes and V_y and $-V_y$ to the remaining two. The voltage applied to the inner electrode is used for motion along the z direction. The tube can be used to scan the sample or the tip.

Carr (1988) has derived the formulas for expansion of the tube ceramic for PZT5H (Vernitron Piezoelectric Division, Bedford, Ohio):

$$x,y = 0.677 \frac{L^{2.066}}{D^{0.767} W^{1.086}}$$

$$z = 2.36 \frac{L^{1.005} D^{0.029}}{W^{1.01}}$$

where x, y, and z are in Å/volt; and L, D, and W are in millimeters. These formulas are accurate for small applied voltages. As the voltage to the ceramic increases, the gain also increases (van de Leemput *et al.*, 1991). The gain increase can be as large as a factor of 2 for an applied voltage of 1000 volts (Jahanmir, 1988).

The motion of the piezoelectric ceramics can be calibrated using an interferometer, a capacitance gage, or a grating. For small scans, atomic corrugations on highly oriented pyrolytic graphite (HOPG) may be used for calibration. A typical calibration curve for a piezoelectric ceramic is shown in Figure

3. As can be seen in Figure 3, the displacement of the ceramic is not a linear function of the applied voltage, and the position of the ceramic for a given applied voltage depends on its past history of movement (hysteresis). Also, the steady-stage position of the ceramic slowly drifts with time (creep). These effects result in image distortion for large scans.

The nonlinearity can be removed either by post-processing of the image (Gehrtz *et al.*, 1988) or by applying appropriate nonlinear voltages to the ceramic. The hysteresis and creep can be reduced by controlling the applied charge to the ceramic (Newcomb and Flinn, 1982) or by placing a small capacitor in series with the ceramic (Kaizuka and Siu, 1988). Kaizuka and Siu (1988) were able to eliminate creep by placing a small capacitor in series with the ceramic. These authors also obtained a factor of 7 reduction in hysteresis. The drawback to this technique is reduction in total dynamic range of the system since the output voltage is now shared between the ceramic and the capacitor.

A correction can also be obtained by a secondary measurement of displacement of the ceramic. The scanner position is monitored as the image is taken and used to correct the distortion induced by the piezoelectric ceramic. Yamada *et al.* (1989) used an optical interferometer to monitor the scans with nanometer accuracy. Griffith *et al.* (1990) have developed a simple capacitance-based position monitor. The scanner position was monitored by capacitors which were mounted near the probe tip on the scanner.

In another effort, Barrett and Quate (1991a) have used a simple two-axis optical beam displacement sensor to measure the x and y position of the piezoelectric tube scanner. The sensor was used for post-image processing and real-time scan correction under feedback control. Post-image scan correction of the data allowed for fast data collection but resulted in some loss of image information due to interpolation errors. In real-time scan correction, the sensor was used to accurately position the piezoelectric scanner for each data point under feedback control. This limited the scan speed and resulted in added noise from the sensor and the control electronics. Using this optical scan-correction system, these authors reported reduction of both linear and quadratic scan distortion to less than 2% of the image size.

Another factor that affects the capabilities of the STM is the resonance frequency of the ceramic. The bending resonance frequency, f_x, and the longitudinal resonance frequency, f_z, are given by (Thompson, 1987):

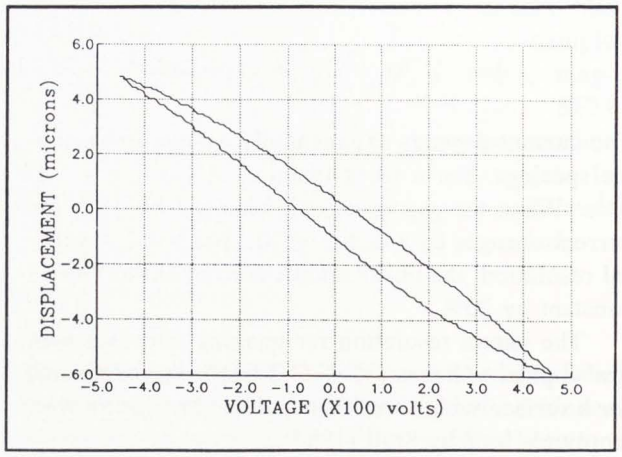

Figure 3. Displacement versus applied voltage for the tube-shaped piezoelectric ceramic. Data were taken with a Michelson interferometer. The motion of the ceramic is nonlinear and has hysteresis.

$$f_x = \frac{0.56}{L^2}\sqrt{\frac{[D^2 + (D - 2W)^2]\,E}{\rho}}$$

and

$$f_z = \frac{1}{4L}\sqrt{\frac{E}{\rho}}$$

where E is the elastic modulus and ρ is the density of the piezoelectric ceramic element. The resonance frequency determines the scanning speed of the microscope and its rigidity against vibration. There is a tradeoff between the range of motion and the resonant frequency. The resonant frequency cannot be increased without the loss of the dynamic range of the ceramic. Also, the addition of any mass to the tube will reduce the resonance frequencies.

Tip Approach

A coarse approach mechanism is required to bring the probe tip from a distance of a few millimeters to within the range of the piezoelectric ceramics. This large dynamic range for the tip approach is achieved differently in vacuum and in air.

The coarse approach in vacuum in early STMs was achieved with a piezoelectric walker named "louse" (Binnig and Rohrer, 1982). The louse is made of a flat piezoelectric material with three metal feet that are insulated from a ground plate with high dielectric-constant material. The sample is mounted

on the piezoelectric material. The louse can be clamped electrostatically to the ground plate by applying a voltage to the metal feet. By elongating and contracting the flat piezoelectric material along with appropriate clamping sequence of the metal feet, the louse can move in any direction on a horizontal plane. Wu and Ng (1991) have implemented a similar piezoelectric walker with electromagnetic clamping that can operate in any orientation.

Another widely used coarse approach mechanism is based on friction and inertia. Pohl (1987) was able to inertially move a mass that was placed on a platform attached to a piezoelectric ceramic. The mass moves forward when an asymmetrically varying voltage is applied to the piezoelectric ceramic. A similar principle was used by Besocke (1987) to move a sample mounted on three piezoelectric tube scanners. The STM tip was mounted on a fourth piezoelectric tube scanner identical to the other three. By mounting the sample on an inclined plane, coarse approach could also be achieved. Another implementation of the inertial coarse approach mechanism, that is commonly used, was developed by Lyding *et al.* (1988). These authors used two concentric piezoelectric tubes. In this design, the inner tube is used for scanning the tip over the sample. The outer tube is used for inertial translation of the sample into tunneling range. The sample is mounted on rails that are attached to the outer piezoelectric ceramic. This arrangement also provides thermal compensation in the z direction. This is in addition to the thermal compensation in the x and y directions due to the symmetric design of the tube scanner.

In air, mechanical devices such as differential screws, stepper motors, or DC motors are used. A mechanical reduction is used to improve the resolution of the motor for tip approach.

Vibration Isolation

Amplitudes of vibrations between the tip and the sample have to be reduced to below the desired resolution of the instrument. This is achieved by rigid construction of the STM and isolation of the system from external vibrations which can excite the relative motion between the tip and the sample.

Sources of vibrations affecting the STM are building vibrations, vibrations caused by the movement of people, and acoustic vibrations. Typical building vibrations are between 10 and 100 Hz, with amplitudes ranging from a few hundred Ångstroms for higher frequency components to several thousand Ångstroms for lower frequency components. These vibrations are produced by equipment running at or near the line frequency and by the associated harmonics. The vibration spectrum of buildings usually contains its largest maxima near the third subharmonic of the line frequency, i.e., 15 to 20 Hz with amplitudes ranging from 1000 Å to 5000 Å (Pohl, 1986).

Other sources of excitations are the irregular vibrations caused by movements of people, which cause frequencies in the 1 to 3 Hz range. The amplitudes for these vibrations are typically similar to the highest amplitude of the building vibrations. The instrument is also susceptible to acoustic vibrations. These vibrations can be reduced by placing the instrument in an acoustic isolation enclosure.

For atomic imaging the amplitude of these vibrations needs to be reduced to less than 0.1 Å. Several methods of active and passive vibration isolation systems have been used with the STM. For use in air, where size and construction materials are not important, a simple and very inexpensive isolation system incorporates a large mass hanging from elastomers. The resonance frequency of this system is inversely proportional to the square root of the stretched length of the elastomer and is kept around 1 Hz. Another vibration isolation system used in air is an air table. Air tables are massive, expensive, and provide poor isolation from horizontal vibrations. In vacuum systems, care must be taken that the vibration isolation system is compatible with ultra-high vacuum (UHV) requirements. The original vibration isolation system used by Binnig *et al.* (1982) was magnetic levitation of the STM on superconducting lead, which was insulated and cooled directly by liquid helium. This system was tedious and difficult to implement. More recent UHV compatible STMs use either a spring suspension with eddy current damping (Binnig and Rohrer, 1982) or a passive system of stacked metal plates separated by Viton spacers and springs (Gerber *et al.*, 1986).

Electronics

In order to keep the tip within the tunneling distance of the surface, a feedback mechanism is employed. The schematic of the electronics for the STM is shown in Figure 4. The tunneling current between the tip and sample is converted to a voltage by a current detection circuit. This voltage is compared with a reference value to produce an error signal. An integrator is used to convert the error signal to an output voltage which adjusts the position of the z-direction ceramic. The tunnel current is then sampled and the feedback loop is repeated. The voltage sent to the z-direction ceramic is stored as a function of x

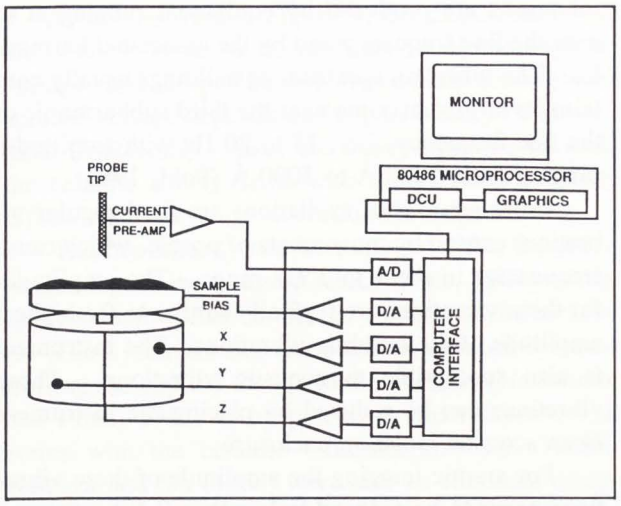

Figure 4. Schematic of STM electronics. A 486 microprocessor and a digital signal processor control the scanning, feedback, data acquisition, and image processing.

---

and y position and related to the topography of the surface.

With the advent of the digital signal processing (DSP) boards, the feedback, x and y scans, data acquisition, and image processing are performed in the computer. This has resulted in significant reduction in complexity of the electronics. Figure 4 is a schematic of the electronics, including the data acquisition and analysis system.

STM Probes

Probe tips are a key component of the STM. They determine both resolution and reproducibility of the results. The image resolution obtained depends both on the radius of curvature and the aspect ratio of the tip. For atomically flat surfaces, only the atoms on the apex of the tip are important. In this application, STM probes can be formed by cutting a piece of wire with cutters. For topographical measurements, images obtained are a convolution of tip shape and surface topography (Griffith *et al.*, 1991).

The images can be deconvoluted from the tip geometry to obtain a more accurate surface topography (Reiss *et al.*, 1990). This is rarely done since the tip geometry is not reproducible and is nearly impossible to measure on a small scale. Therefore, high aspect ratio probes with small radii have to be used to minimize the convolution effects.

The STM tips are usually made from either tungsten or platinum-iridium wires. Tungsten is mechanically rigid but it tends to oxidize. Pt/Ir is less rigid, but it is inert both in air and in solutions. The predominant methods of producing tips are mechanical cutting/grinding and electrochemical etching. For electrochemical etching of W, solutions of NaOH or KOH have been used. In etching Pt/Ir wires, solutions of $CaCl_2/H_2O/HCL$ (Musselman and Russell, 1990), $NaNO_3/NaCl$ (Nishikawa *et al.*, 1988), and NaCN/KOH (Heben *et al.*, 1988) have been used. Melmed (1991) has compiled the many techniques for making sharp tips.

The most widely used technique for tip preparation is the electrochemical etching of tungsten as follows:

Anode: $W(s) + 8OH^- \text{-----} > WO_4^{2-} + 4H_2O + 6e^-$

Cathode: $6H_2O + 6e^- \text{-----} > 3H_2(g) + 6OH^-$.

Solutions of potassium or sodium hydroxide are used for this purpose.

The voltage applied between the electrodes can be either AC or DC. The voltage between the AC-method is a self-terminating technique which makes conical tips with the radius dependent on the original diameter of the wire used, the solution, and the applied voltage. These tips are made by inserting a section of tungsten wire a few millimeters into the solution. An AC voltage of approximately 6 volts is then applied between the wire and the second electrode in the solution. The etching stops when the tip has been formed and does not touch the solution any longer. For a 10 mil tungsten wire, the radii obtained range from 3000 to 5000 Å (Figure 5).

A sharper tip with a lower aspect ratio can be obtained by applying a DC voltage between the electrodes (Ibe *et al.*, 1990). During this etching process, the bottom part of the electrode is somewhat shielded from the electrochemical etching process by the heavy products of the reaction at the top (Figure 6). This causes formation of a cusp near the top of the wire in the solution. The reaction continues at a faster rate at the cusp than the lower part of the electrode. Eventually, the weight of the electrode at the bottom of the cusp exceeds the tensile strength of the wire at the cusp and the bottom part drops off. An electronic circuit senses the change in voltage across the electrodes and shuts off the etching process. The radius of the tip depends on the switching speed of the electronic circuit and is usually less than 1000 Å (Figure 7).

Various researchers, e.g., Biegelsen *et al.* (1987) have indicated the possibility of oxidation of as-prepared tungsten tips. Auger electron spectroscopy of

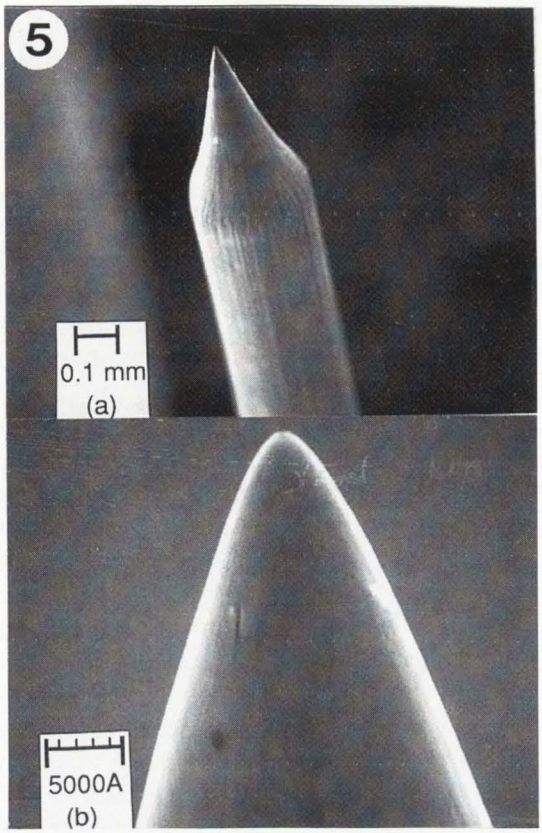

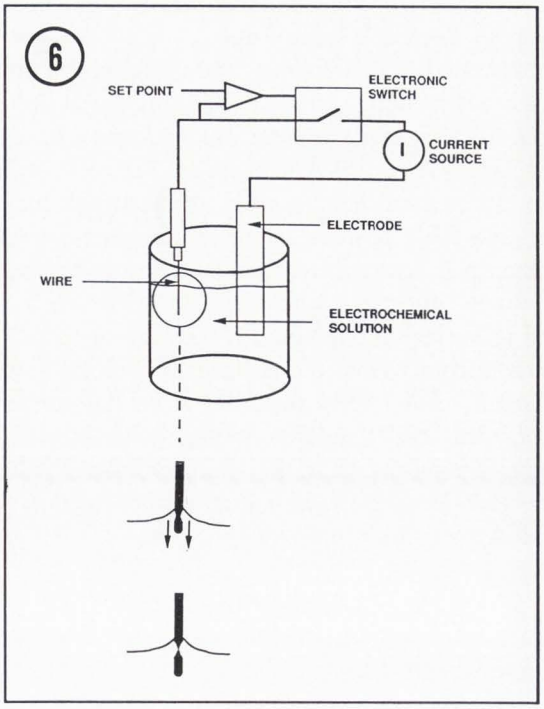

Figure 6. Schematic representation of the apparatus used for etching tungsten wires with the DC-method. The inset shows the formation of the cusp and the final tip formation.

Figure 5 (at top left). SEM photographs of a tip made by electrochemically etching a 0.25 mm tungsten wire using the AC-method shown at two different magnifications.

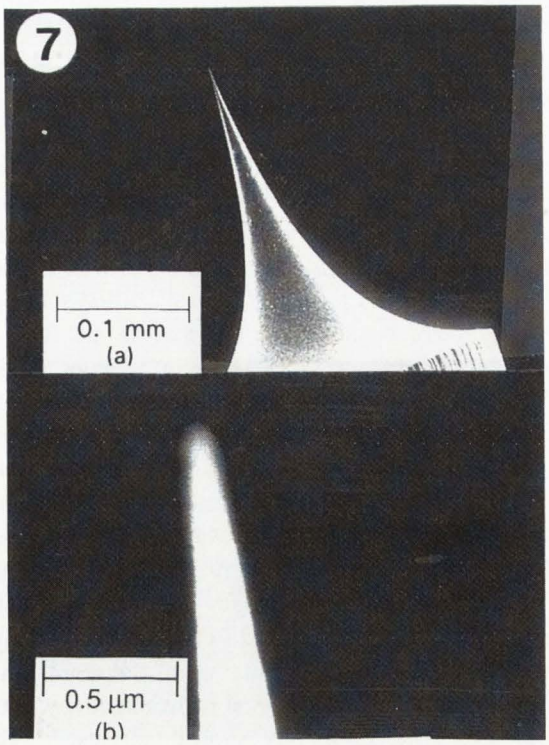

Figure 7 (at bottom left). SEM photographs of electrochemically etched 0.25 mm tungsten wire by DC-method shown at two different magnifications.

---

the tips has indicated the presence of oxygen and carbon with almost no tungsten signal at the surface (Chiang and Wilson, 1986). Other contaminants such as organic adsorbates and alkali metal salts (Colton *et al.*, 1987) may also be present. Most researchers have indicated the necessity of a post-preparation processing of the tips, such as focused ion milling (Vasile *et al.*, 1991), electron bombardment (Demuth *et al.*, 1986), high electric field desorption and/or evaporation (Stroscio *et al.*, 1987), heat treatment (Binh, 1988), high voltage pulses, and in an extreme case, tip crash into the surface (Schneir *et al.*, 1986).

Modes of Operation

The STM can be operated in two different modes: constant current and constant height. In constant cur-

rent mode, the tip-to-sample current is kept constant through a feedback control unit.

Operated in this manner, the tip moves in the x, y, and z directions, following the topography of the surface. This mode is used predominantly for scan sizes larger than 100 Å to measure surface topography. In constant height mode, the feedback loop is open and the z position of the tip remains constant. As the tip is scanned over the surface, tip-to-sample current is collected. The variation in current is related to surface topography. Since the tip is only a few Ångstroms from the surface, this mode is used for small scans of less than 100 Å on flat surfaces. In practice, the z motion of the tip is allowed to change slowly by using the feedback system with a very low loop gain which allows correction for thermal drift and sample tilt.

Applications

Atomic Orientation

Since the initial report of real-space atomic resolution images of the 7x7 reconstruction of Si(111) (Binnig *et al.*, 1983a), STM has been applied as a surface science probe in the investigation of surface properties of numerous materials (Quate, 1986; Hansma and Tersoff, 1986; and Feuchtwanga and Cutler, 1987). These include the atomic structure of GaAs(110) (Feenstra and Fein, 1985), 5x5 surface reconstruction on Ge-Si(111) (Becker *et al.*, 1985a), reconstructed platinum surface (Behm *et al.*, 1986), germanium surface reconstructions and phase boundaries (Becker *et al.*, 1985b), the spatial variation in superconductivity of Nb_3Sn (de Lozanne *et al.*, 1985), and 2 degree vicinal Si(001) shown in Figure 8 (Griffith and Kochanski, 1990).

The STM has also been used to study adsorption on surfaces. The atomic arrangement of sulfur atoms on Mo(001) at atmospheric pressure was studied by Marchon *et al.* (1988). Other studies include Ga adsorption on Si(100) (Nogami *et al.*, 1990), adsorption of boron on Si(111) (Avouris *et al.*, 1990), and Ag, Cu, Pd, and Si on Si(111) and Si(100) (Neddermeyer, 1990).

Atomic resolution images can now be routinely obtained. Images of carbon atoms on highly oriented pyrolitic graphite (HOPG) can be easily obtained in air (Figure 9, on color plate at page 637), liquids, and vacuum. Real-space atomic resolution images of the 7x7 reconstruction of Si(111) (Figure 10) as well as other surfaces can easily be measured in UHV.

Spectroscopy

The high resolution capability of the STM can be applied to tunneling spectroscopy and electronic measurements of surfaces. These measurements are concerned with the study of the local electronic density of states of materials. The STM provides the opportunity to perform combined microscopic and spectroscopic measurements on the same local area. This combination has been successfully demonstrated on metals, semiconductors, and superconductors. Kaiser and Jaklevic (1986) used the STM to study the electronic surface states on Au(111) and Pd(111). In semiconductor applications, both GaAs and Si surfaces have been studied. Feenstra and Stroscio (1987) used tunneling spectroscopy to study p-type, n-type, and oxygen-covered GaAs(110) surfaces. On silicon, Kaiser *et al.* (1988) characterized the electronic properties of the hydrogen-terminated surface, using an STM in a nitrogen ambient. Elrod *et al.* (1986) used low temperature tunneling microscopy and spectroscopy to study the superconducting properties of a niobium-tin alloy film. Shih *et al.* (1990) studied the properties of metal films with thicknesses in the range of 1 to 10 monolayers on GaAs (110). They found a layered structure for Sb films. The films were found to be semi-metallic with a very low conductivity at the Fermi-level. The Sn films went through a structural phase transition along with an electronic transition from semimetallic to metallic above two monolayers of coverage.

Feenstra and Slavin (1991) have studied the structural and electronic properties of cleaved and annealed Ge(111) surfaces. These authors studied the voltage-dependent imaging of the *c*2x8 structure. The Ge surface atoms occupy two types of sites called "adatoms" and "rest atoms." The empty states of the surface are centered on the adatoms (blue in Figure 11, on color plate at page 637) and the filled states of the surface are centered on the rest atoms (red in Figure 11, see page 637). The empty states of the surface were imaged with the STM tip negative with respect to the sample, and the filled states were imaged with the tip positive. The two images were combined to produce a direct view of the surface.

The surface of GaAs(110) was similarly imaged by Feenstra *et al.* (1987). Figure 12 (a) and (b) show the constant-current STM images of the surface with sample voltages of +1.9 and -1.9 V, respectively. Figure 12 (c) shows the orientation of the atoms on a Ga(110) surface with As atoms represented by open circles and Ga atoms by closed circles. The combined image of occupied and unoccupied states is

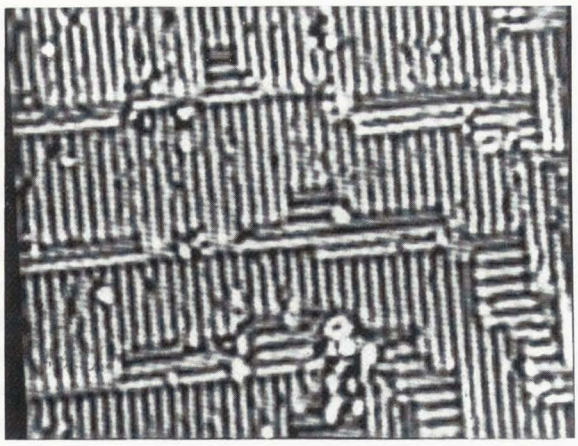

Figure 8. STM image of 2 degree vicinal Si(100). Single steps dominate the surface. The shading is keyed to surface curvature. (Photo courtesy of J.E. Griffith).

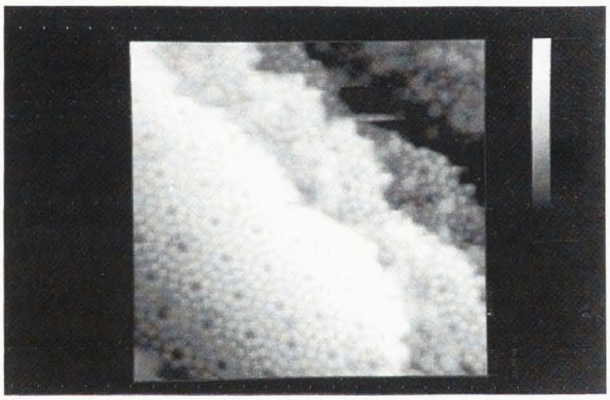

Figure 10. A 200 Å x 200 Å STM image of the Si(111)-7x7 reconstruction. The image was taken in a constant current mode with an UHV-STM. (Photo courtesy of Burleigh Instruments).

Note: Figures 9 and 11 are on color plate at page 637; Figure 13 is on color plate at page 638.

---

shown in Figure 13 (on color plate at page 638).

Comparison with the theoretical state-density contours shows that the occupied state density is concentrated around the surface As atoms and the unoccupied density around the Ga atoms.

Electrochemistry

Tunneling microscopy is not limited to vacuum or air and may be performed in liquids, expanding the applications to electrochemistry and corrosion studies.

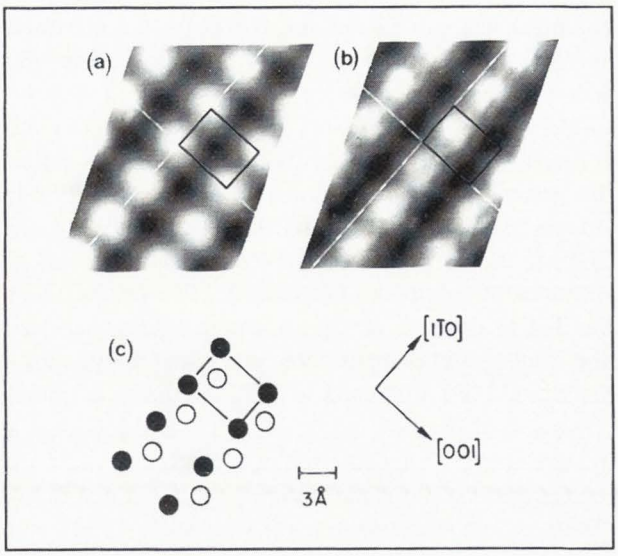

Figure 12. Constant-current STM images of GaAs(110) acquired at sample voltages of: (a) +1.9 V and (b) -1.9 V. Surface height is given by a gray scale, ranging from 0 (black) to (a) 0.83 Å and (b) 0.65 Å (white). (c) Schematic representation of surface atoms showing the position of Ga (open circles) and As (closed circles) atoms. The rectangle shows the unit cell in all three figures. (Photo courtesy of R.M. Feenstra).

The first use of STM in electrochemistry was demonstrated by Sonnenfeld and Hansma (1986). These authors demonstrated atomic resolution images of HOPG in water and the topography of a gold surface in a sodium chloride solution. Robinson (1988) performed tunneling microscopy in the presence of an externally applied electrochemical current. Lev *et al.* (1988) imaged electrode surfaces under potentiostatic control. They used a four-electrode STM and were able to decouple the tip-sample bias from the sample potential. Wiechers *et al.* (1988) observed modification of terraces on a Au electrode due to Cl^- absorption. The electrode was imaged in an aqueous solution of 0.05 M H_2SO_4 and 5 mM NaCl. Trevor *et al.* (1989) studied the roughening and dissolution of epitaxially grown Au(111) film on mica. They correlate the terrace structure changes to the oxidation and reduction cycles in 0.1 M $HClO_4$. Other investigators have studied electrodeposits on conductive surfaces. Green *et al.* (1988) observed *in-situ* deposition and stripping of an electrochemical film. Single steps of Au(111) were imaged during the deposition and stripping of a monolayer of Pb in an acid electrolyte.

In the STM applications in solutions, the tunnel-

ing current is non-faradaic and does not contribute to chemical changes in the solution or at the substrate surface. The faradaic currents that result from the redox processes at the tip and sample can also be used to control the motion of the electrode over the substrate. This implementation of the STM is called the scanning electrochemical microscope (SECM) (Kwak and Bard, 1989, and Bard *et al.*, 1989). In SECM, the current is controlled by electrochemical reactions at the tip and the sample. The resolution of the SECM depends on tip-to-sample spacing, tip size and shape, solution resistance, and mass/charge transfer rates. The tips used in SECM consist of metal wires sealed in glass capillaries with radii less than a micrometer. Applications of the SECM include measurements of surface topography (Kwak and Bard, 1989), potential distributions (Kwak *et al.*, 1990), and microfabrication (Craston *et al.*, 1988, and Mandler and Bard, 1990).

In application of the STM to electrochemistry, the tunneling tips have to be insulated leaving only the apex exposed to the solution. The insulation has to be inert in the electrochemical solution. Different methods have been used to insulate the tunneling tip and minimize the faradaic currents. Schneir *et al.* (1988b) insulated their tunneling tips by depositing 100 nm thick SiO in a vacuum chamber. They removed the SiO from the apex of the tip by field emission in an STM. To insulate their tips, Nagahara *et al.* (1989) used Apiezon wax which was inert in various electrolytes. They reported leakage currents as low as 0.1 nA in 0.1M $HClO_4$ with a tip bias of 0.1 V. Gewirth *et al.* (1989) coated their tips by dipping them into a solution of varnish and solvent. The tip was then set in an upright position and the varnish was allowed to run off the tip. The degree of coating was controlled by varying the dilution of the varnish and the sharpness of the tip. Other coatings include glass (Heben *et al.*, 1989) and polymers (Penner *et al.*, 1989).

The electrode/electrolyte interface plays a central role in electrochemical systems. The use of STM and SECM for *in-situ* studies of the electrode surfaces will provide insight into geometric and electronic features of these materials. Further advancements in producing insulated tunneling tips and ultramicroelectrodes will pave the way for the future developments in the application of the STM/SECM to electrochemistry.

Nanofabrication

A major application of the STM is to induce local modifications of surfaces. Potential uses include nanolithography, metal deposition, etching of semiconductors, micromachining, and data storage.

The microprocessing of surfaces may be performed by mechanical, thermal, electrical, or chemical means. Abraham *et al.* (1986) performed lithography by scratching the surface with the tip in the STM. The surface was then imaged with the STM. The result was a feature that was 150 Å across and 30 Å deep, which relaxed into a Y-shaped feature after 13 minutes. They were also able to produce hillocks that were 200 to 250 Å wide and 20 Å high by increasing the tunneling current to 1 microamp. They correlated these results to gold transfer from the tip to the sample. This gold was transferred to the tungsten tip during previous experiments. A similar experiment was performed by van Kempen and van de Walle (1986). They observed an indentation of approximately 40 Å deep after pressing a tungsten tip into an Ag(001) surface. Also, McCord and Pease (1987a) used the STM as a micromechanical tool to directly cut lines in 200 Å films of CaF_2 and AlF_3.

Although contact lithography is capable of producing high resolution features, the results are not reproducible because of the tip changes occurring during contact. Non-contact lithography may be performed by using the STM to induce chemical changes on surfaces of materials.

Ringger *et al.* (1986) have formed lines that were approximately 20 Å wide on glassy $Pd_{80}Si_{19}$ substrates without the tip touching the surface. They found that the observed line contrast, measured by a scanning electron microscope (SEM), was due to the increase in the secondary electron yield rather than the result of a topographical change. They suggest that a local chemical transformation of an adsorbate contamination layer plays an important role in this lithographic process. The presence of a hydrocarbon film on these surfaces, arising from diffusion pump oil, was confirmed by X-ray photoelectron spectroscopy (XPS) measurements.

Lithography was also done on an atomically flat surface of gold covered with a layer of fluorocarbon grease (Schneir *et al.*, 1988a). Features with dimensions as low as 100 Å were formed on atomically flat surfaces of gold prepared in air by melting a gold wire with an oxyacetylene torch. These features were unstable and were distorted within an hour of being formed. This distortion was related to the surface diffusion of gold. They were not able to reproduce these results in air.

Formation of lines on contamination layers was

also investigated by McCord and Pease (1986). By applying 10 volts between the tip and the sample, they were able to produce contamination tracks on 1000 Å films of gold on silicon substrates. The line widths were estimated to be less than 1000 Å. In the same paper, they also reported the first lithographic application of STM to Langmuir-Blodgett films.

In another effort, the possibility of local crystallization of the glassy state or Taylor cone formation of the locally molten surface on $Rh_{25}Zr_{75}$ substrate has been postulated (Staufer *et al.* 1987). These authors were able to obtain hillocks and lines that were approximately 350 Å wide and 100 Å high by increasing the bias voltage to 1.5 volts. In another effort, Staufer *et al.* (1991) analyzed the response of different glassy metals to nanostructure fabrication processes. Their results agreed with the theory of local heating.

A demonstration of the ultimate capability of the STM as a nanofabrication tool was performed by Eigler and Schweizer (1990). The authors spelled "IBM" using xenon atoms on a nickel single crystal surface. The physisorbed atoms on the nickel surface were moved by the STM tip and arranged so that they spelled "IBM". The surface was then imaged using the STM. The process is shown in Figure 14.

In the above experiments, the application of the STM to local modification of surfaces was demonstrated. McCord and Pease have demonstrated the use of STM for lithography on thin films of calcium fluoride (McCord and Pease, 1987b) and poly(methylmethacrylate) (PMMA) (McCord and Pease, 1988). On calcium fluoride, they induced dissociation of the molecules and formed 200 Å wide lines by using a 20V, 2 nA beam. The lines were developed in water and imaged by SEM. Analogous line widths were obtained on PMMA films using electron energies of 20 to 30 eV and doses $> 10^{-2}$ C/cm^2. The PMMA films were developed after exposure and used for metallization of the underlying substrate. These metal lines were then imaged by SEM.

More recently, Marrian *et al.* (1990) have used STM to expose e-beam resist. These authors used bias voltages of 8 to 35 volts to write features as small as 20 nm on the resist. Dobisz and Marrian (1991) have obtained feature sizes of 25 to 45 nm on negative e-beam resist using voltages of 15 to 35 volts in a vacuum STM (Figure 15). Marrian and Dobisz (1991) have also modified a thin film of P4BCMU e-beam resist (polydiacetylene with urethane substituents) using STM. They wrote dots of about 12 nm wide and 6 nm high using 8.5 volt pulses. The dots were combined to form the letters NRL (Figure 16). The surface was then imaged with STM.

Etching of semiconductor surfaces has been performed by STM in an electrochemical cell. Nagahara *et al.* (1990) controllably etched nanometer size features into Si(100) and GaAs(100) surfaces using STM in an etching solution. They were able to etch features as small as 20 nm in a dilute (0.05%) HF solution. They speculate that the surfaces were oxidized due to the high local electric field under the tip. The oxide was then dissolved in the HF solution.

High resolution etching of metals and semiconductors and electrodeposition of metals have been demonstrated with the SECM. Lin *et al.* (1987) etched submicron lines on n-GaAs in an aqueous solution of NaOH and EDTA with simultaneous irradiation by a tungsten-halogen lamp. Mandler and Bard (1990) used SECM to etch GaAs, GaP, CdTe, and $Hg_{1-x}Cd_xTe$. Strong oxident, Br_2, was electrogenerated *in situ* at the ultramicroelectrode in a solution of 0.02M HBr and 0.5M HCl and used as the etchant. The sizes of the etched pits depended on the tip-to-sample spacing, the size of the tip, and the solution composition. The SECM was also used to deposit and etch metals. Husser *et al.* (1989) deposited and etched submicron patterns of silver, copper, and gold. These authors used different ionically conducting polymers such as in Nafion, poly(4-vinylpyridine), and poly(bis-(methoxyethoxide) phosphazene) on the substrate as the electrochemical media.

The STM has also been used for direct deposition of metallic features from an organometallic gas. Ehrichs *et al.* (1988) used the STM to directly write cadmium features as small as 200 Å on copper and silicon substrates in a dimethylcadmium gas environment. In another study, McCord *et al.* (1988) reported fabrication of metallic lines on silicon substrates with features as small as 100 Å by operating the STM in the field emission mode in an organometallic gas ambient. They observed a deterioration in the line resolution due to metal deposition on the tip.

Mamin *et al.* (1990) showed that gold tips can be used as a solid-state emission source by field evaporation. Mounds of gold were deposited on a Au(111) surface with pulses of 3.5 to 4 volts and 10 to 600 ns duration. The mounds were typically 100 to 200 Å diameter and 20 to 30 Å high. They used the STM to write several thousand mounds without any observed degradation in the tip's ability to emit atoms. Mamin *et al.* (1991) showed that the structures were stable for weeks and at elevated temperatures.

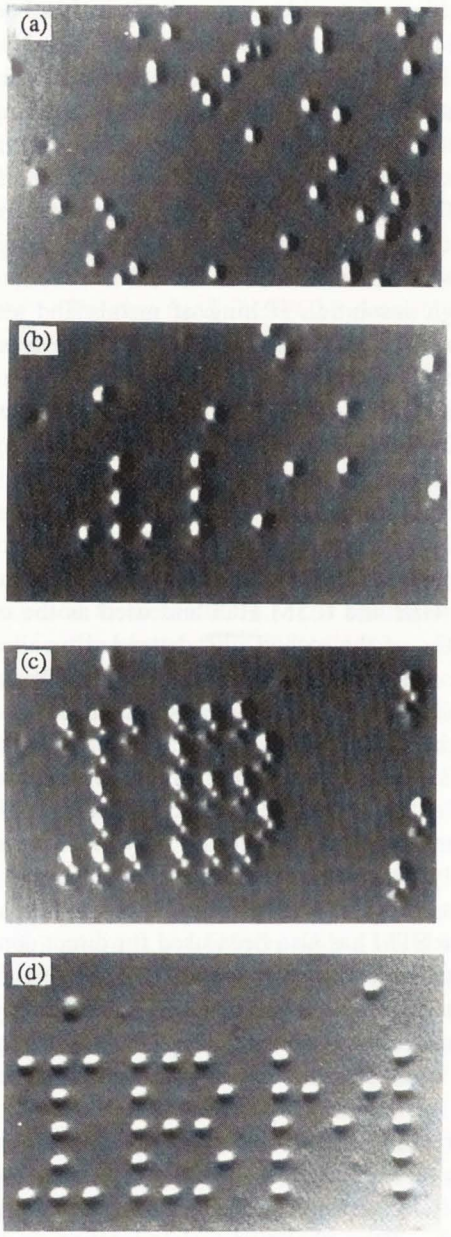

Figure 14. A sequence of STM images taken during the creation of the letters "IBM" on a nickel surface. The xenon atoms were moved across a nickel (110) surface using the STM. Image (a) shows xenon atoms scattered on the surface. Images (b) and (c) show the intermediate steps as the atoms are moved into position. Image (d) is the completed pattern showing the letters "IBM". (Photos courtesy of IBM Research Division, Almaden Research Center, San Jose, California).

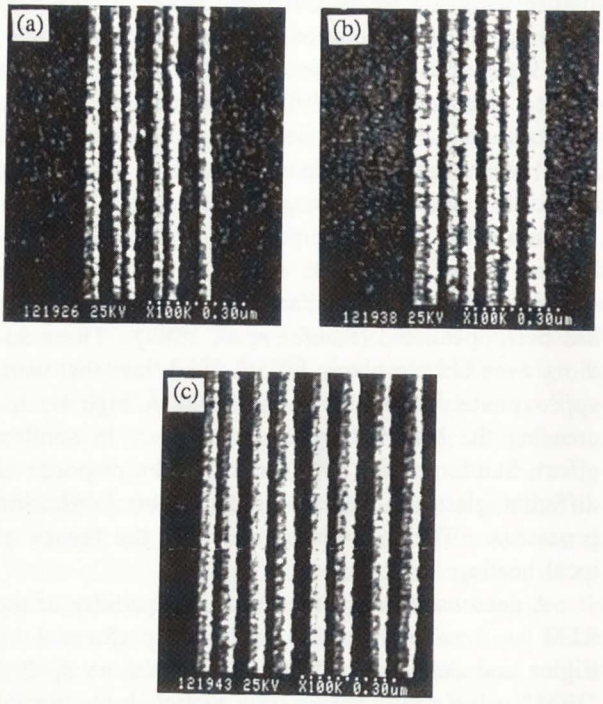

Figure 15. SEM photographs of line patterns on 60 nm resist. The lithography was performed with an STM. The feature sizes depend on the writing voltage. The line-widths are (a) 25, (b) 35, and (c) 45 nm for applied voltages of 15, 25, and 35 V, respectively. (Photo courtesy of C.R.K. Marrian).

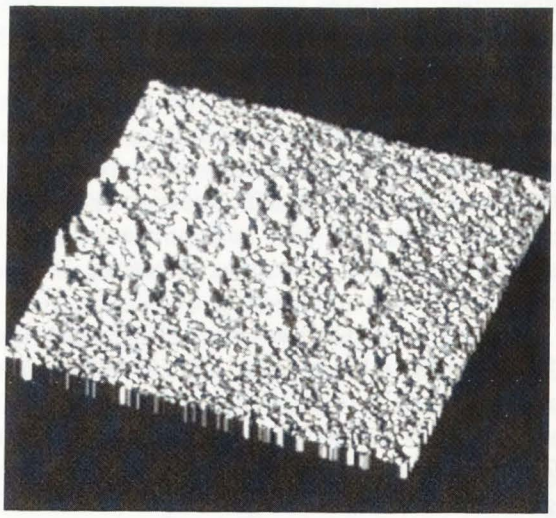

Figure 16. STM image of a thin film of polydiacetylene, P4BCMU. The film was modified lithographically in an STM. Each dot is about 20 nm wide and 8 nm high. (Photo courtesy of C.R.K. Marrian).

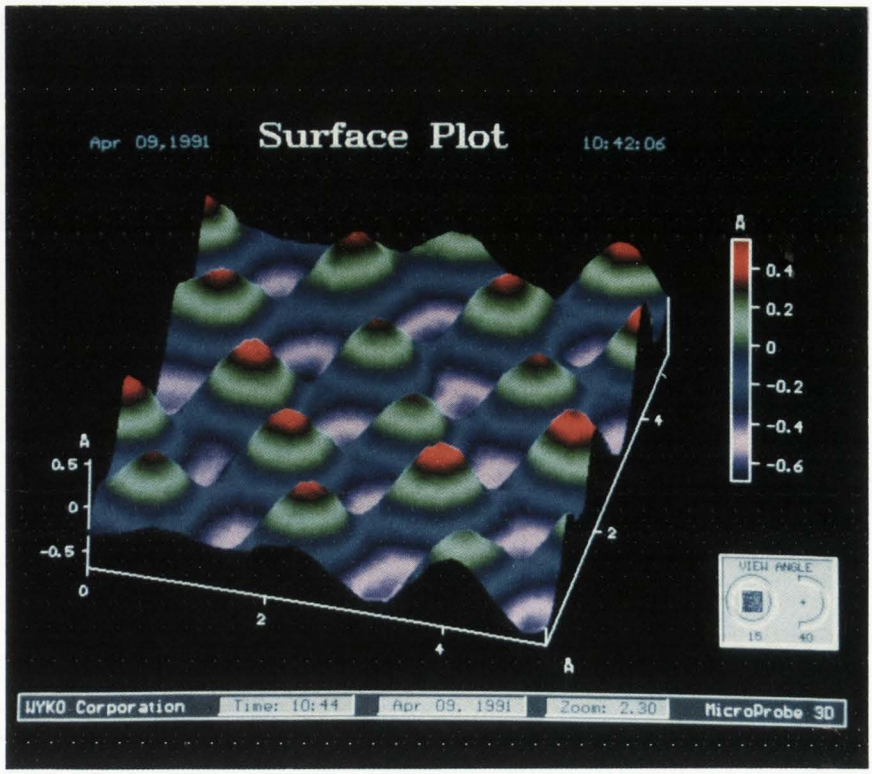

Figure 9. STM image of a highly oriented pyrolytic graphite surface. The image was taken in constant height mode in air.

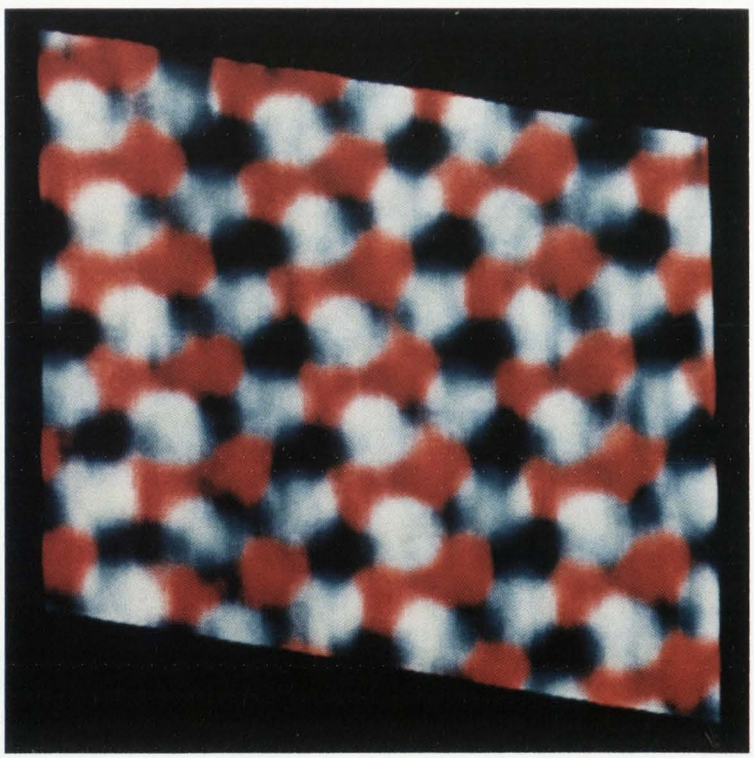

Figure 11. Combined color STM images of the Ge(111) surface with a c2x8 reconstruction. The Ge surface atoms occupy two types of sites called "adatoms" and "rest atoms". Empty states of the surface are centered on the adatoms. Filled states of the surface are centered on the rest atoms. The image of adatoms was acquired by tunneling into the empty states (blue) and the image of rest atoms was obtained by tunneling out of the filled states (red). Combining the images produces a direct view of the entire surface structure. (Photo courtesy of R.M. Feenstra).

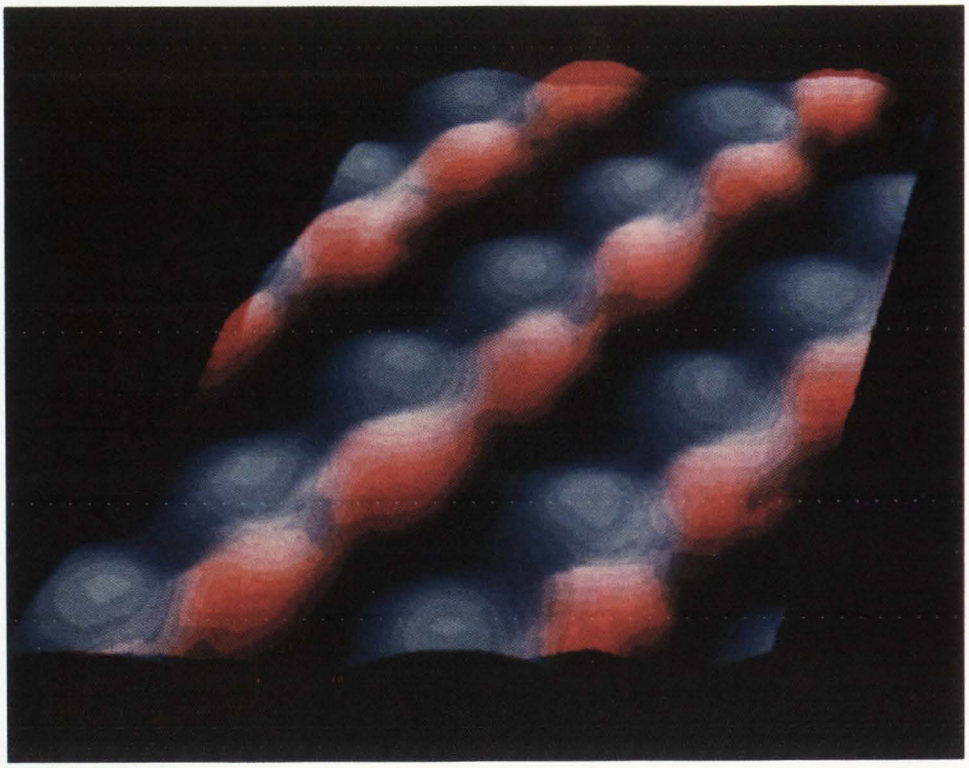

Figure 13. Combined STM images of the GaAs(110) surface, showing the Ga atoms and As atoms. The image of Ga atoms was acquired by tunneling into empty states which are localized around surface Ga atoms (blue). The image of As atoms was acquired by tunneling out of filled states which are localized around surface As atoms (red). (Photo courtesy of R.M. Feenstra).

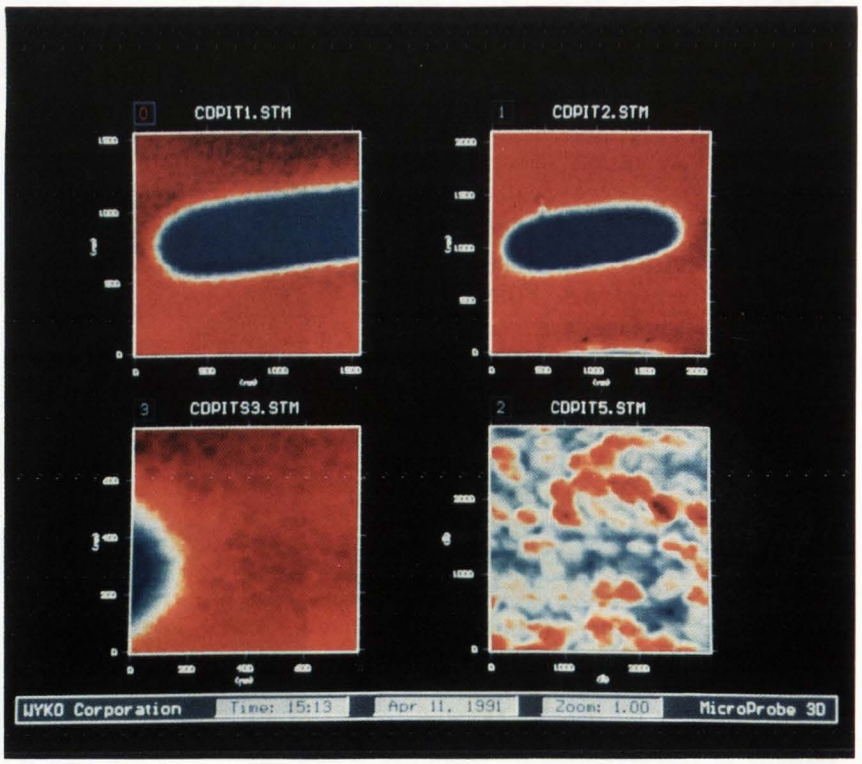

Figure 17. STM images taken on a gold coated compact disk. The scan sizes are 2000x2000 nm, 1500x1500 nm, 800x800, and 300x300 nm. The gold grains are visible on the surface.

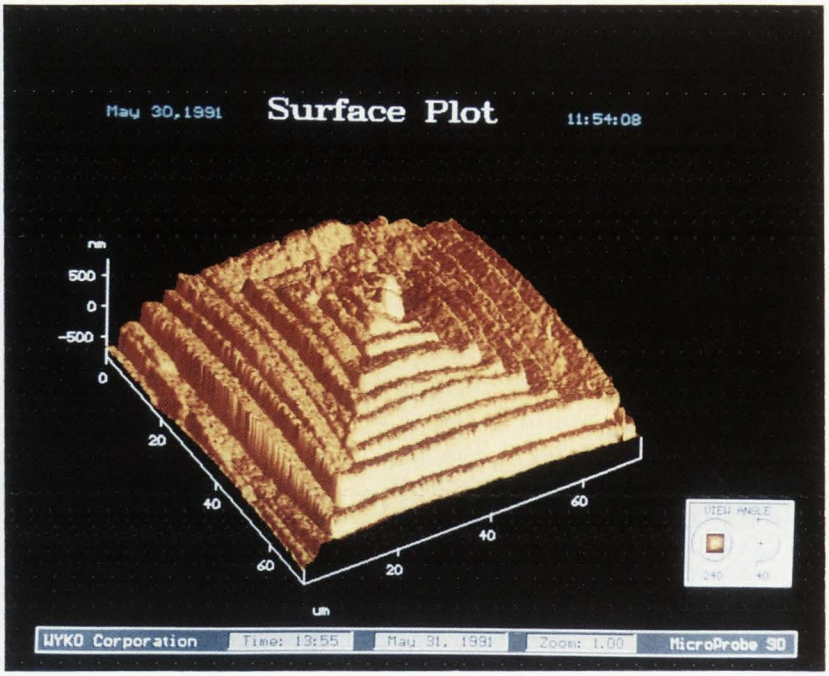

Figure 27. An SFM image of a diamond crystal grown on a circular seed crystal. The scan size is 70x70 μm. (Diamond sample courtesy of K. Snail and C. Marks).

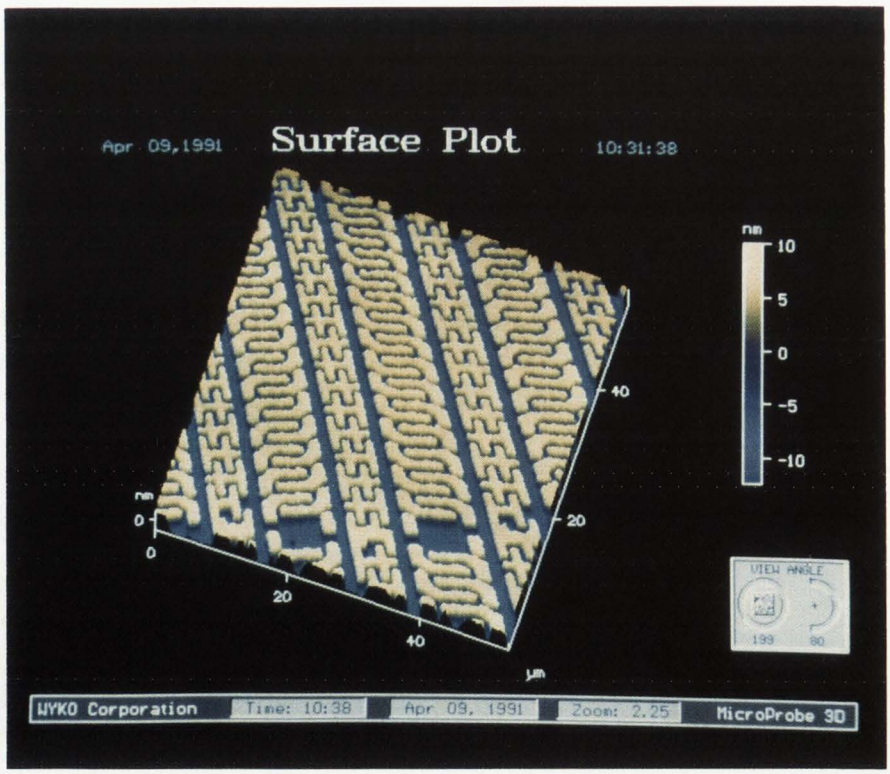

Figure 28. An SFM image of a test pattern on an integrated circuit. The scanned area is 50x50 μm.

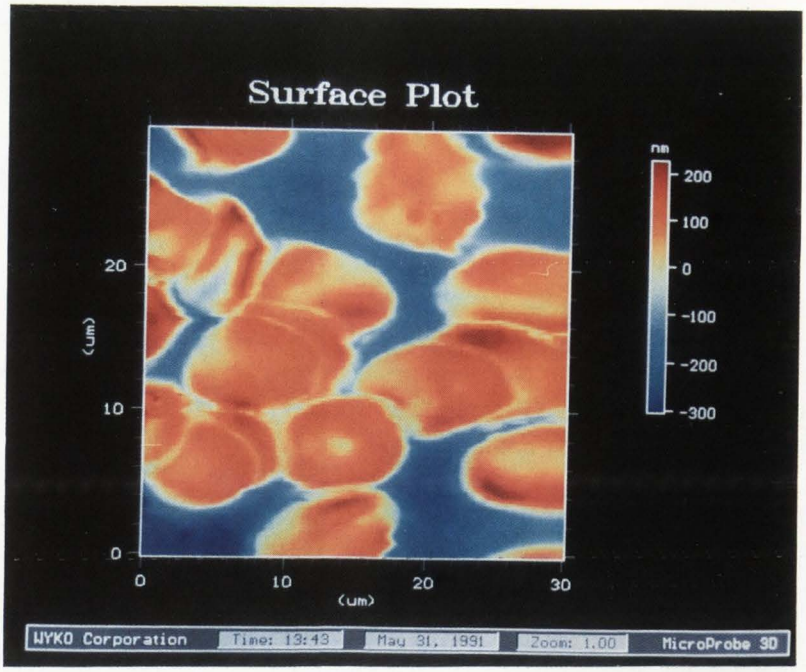

Figure 31 (at right). An SFM image of blood cells. The sample was prepared by simply putting a small drop of blood on a glass slide and air drying for 30 minutes. The scan size is 30x30 μm.

Figure 35c (see Figures 35a and 35b on page 653; Figure 35c below). An image of a Nuclepore membrane filter taken with the scanning ion-conductance microscope. The pores are 0.8 μm in diameter. The scan size is 7.8x4.5 μm. (c) The image of ion currents from the pores taken with the scanning ion-conductance microscope. (Photos courtesy of P. Hansma and G. Kelderman).

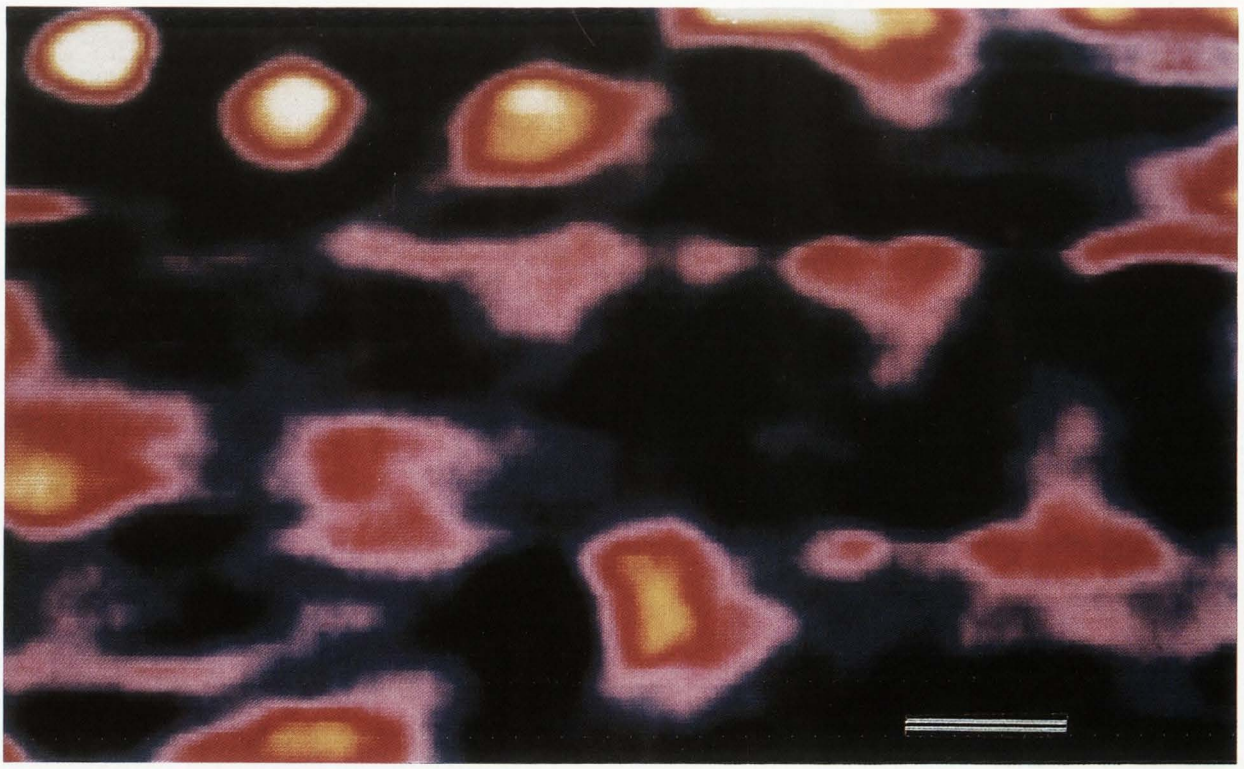

Dagata *et al.* (1991) have brought the STM one step closer to being used as a tool for electronic device processing. These authors used the STM to form ultra-shallow (2 nm) oxide features on silicon by adjusting the bias voltage between the tip and the sample in the presence of oxygen. The patterned silicon was used in a subsequent processing step for selective-area gallium arsenide molecular beam epitaxy (MBE). The patterned oxide withstood the temperature cycling up to 800 °C, required for MBE.

It is clear that the STM can be used for nanolithography, metal deposition, and etching. But the processes already discussed are too slow to be used in manufacturing of integrated circuits. With further development, the STM could be used in special device processing where quantity and speed are not required.

Biological Materials

The possibility of applying the high resolution of the STM to the study of biological materials is intriguing. Many studies have been performed on DNA molecules with varying success. Researchers (Barris *et al.*, 1988; Lindsay *et al.*, 1988; and Lindsay *et al.*, 1989a,b,c) have demonstrated the ability to image DNA molecules in an aqueous solution with molecular scale resolution. Also, Amrein *et al.* (1988) obtained images of freeze-dried recA-DNA complexes coated with a conducting metal film. The STM resolved the number of recA monomers per helical repeat of the complex.

STM images have also been taken on uncoated DNA samples in air (Lee *et al.*, 1989; Dunlap and Bustamante, 1989). Beebe Jr. *et al.* (1989) imaged double-stranded DNA and were able to distinguish major and minor grooves. Arscott *et al.* (1989) studied the Z-DNA with the STM. Their measurements of the general structure and helical parameters agreed with models derived from x-ray diffraction. Li *et al.* (1991) obtained STM images of B- and Z-DNA. On B-DNA, major and minor grooves could be distinguished. On Z-DNA, the left handedness of the helix was identified.

One of the most promising results on DNA has recently been obtained by Driscoll *et al.* (1990). These authors obtained real space atom-resolved images of double-helical DNA using STM in an ultra high vacuum environment. The DNA was deposited on HOPG without further processing. The experimental STM profiles correlated with the modeled contours of the van der Waals surface of A-DNA (Youngquist *et al.*, 1991).

Large molecules have also been imaged with STM. Edstrom *et al.* (1991) used the STM to image the uncoated components of the skeletal muscle glycogenolytic complex in air. The images they obtained correlated well with the known features of the molecules except that the measured height was 30% of the true thickness. The discrepancy in height could be the result of the forces exerted on the molecules by the tip. Masai *et al.* (1991) have also imaged large, uncoated fibrous actin polymers from muscles. The structural features of the F-actin paracrystals were consistent with those measured with a transmission electron microscope. Welland *et al.* (1989) have imaged the globular protein vicilin molecules. Their measurements correlated with the overall shape deduced from x-ray scattering. In another study, Edstrom *et al.* (1989) used STM to image phosphorylase kinase and phosphorylase b, which are protein molecules. The images of phosphorylase b were consistent with measurements based on other techniques. The images of phosphorylase kinase gave thickness values that were one-fourth to one-half of the expected value.

Large molecules have also been imaged in solutions (Lindsay, 1989). Mainsbridge and Thundat (1991) used the STM to image grana and lamellae of spinach chloroplasts directly in a buffer solution. The samples were electrochemically deposited on a gold substrate while in the buffer solution. They observed the possible contact sites on the membrane surface where the proteins are imported selectively into the membrane.

STM measurements have been performed on large molecules that were coated with a conductive film. Amrein *et al.* (1991) used the STM images to complement their measurements with the transmission electron microscope. The STM measurements were performed on freeze-dried and metal-coated protein layers. Three-dimensional images of the structural details of the individual protein complexes were obtained. Blackford *et al.* (1991) have imaged large molecules that were coated. The images were obtained on hoop-shaped components separated from the cell sheath by chemical treatment.

Although extensive progress has been made in imaging biological molecules with STM, the theoretical basis for the conduction and contrast mechanism is not well understood. The molecular adsorbates are generally nonconductive, but in most cases sufficient contrast can be obtained in STM measurements. Only a few attempts have been made in explaining this discrepancy. Lindsay *et al.* (1988) have indicated that the adsorbate deformation plays a role in

contrast mechanism. Keller *et al.* (1989) and Salmeron *et al.* (1990) have suggested a model where the electron tunnels from the tip into a weakly adsorbed molecule. The electron propagates in through the molecular potential well and then tunnels to the substrate. The tunneling probability is enhanced when resonant tunneling occurs for some values of the electron energy. Similarly, Lindsay *et al.* (1990) have proposed a model in which tunnel conduction is enhanced by resonance effects. The resonant tunneling enhancement occurs when the Fermi energy of the molecule is close to the Fermi energy of the electrodes. Lindsay *et al.* (1990) propose that this occurs due to the pressure exerted by the STM tip. Yuan and Shao (1990) have suggested a model which indicates that quantum interference electrons are an important factor in the contrast mechanism of biological molecules. These authors point out that the observed contrast patterns may not be directly interpreted as the structures of the molecules.

Also, care must be taken when using HOPG as a substrate for STM imaging of organic and biological materials. Chang and Bard (1991) obtained images of features which covered 1% to 10% of the cleaved HOPG surface. Images included cleavage steps, single and double stranded graphite structures stretched over a few micrometers, graphite fibers, ultrasmall carbon particles of 5 to 10 Å diameter, and broken graphite pieces forming star-like features. Clemmer and Beebe Jr. (1991) measured periodic features on the cleaved surface of HOPG with periods in the range of 18 to 53 Å. Some of these features could be confused with DNA. These authors also found features with nonuniform sizes which resembled structures of biological molecules.

It is clear that the STM can be an extremely useful tool in biochemistry. But, further progress in the application of STMs to biological materials will require a better understanding of the conduction and contrast mechanism. Improved sample preparation techniques and the selection of suitable substrates that are free of artifacts are also necessary.

Topography

The STM has also been used as a metrology tool. The STM has been applied to topographical mapping of a grating replica and a diamond-turned surface (Dragoset *et al.*, 1986). Surface structures on a diamond-turned gold mirror were observed which were not detected with other techniques. Figure 17 (see color plate at page 638) is an image of a compact disk showing the data bits and the grain structure of the gold thin film. In Figure 18, the tracks and grain structure were measured on a magnetic disk. The unprecedented resolution of the STM can be used to map and understand the surface roughness and structure of thin films, diamond-turned surfaces, and mirrors for X-ray and UV applications. Future development of higher aspect ratio probes (Vasile *et al.*, 1991) and encoder based scanners (Griffith *et al.*, 1990, and Barrett and Quate, 1991a) will lead to applications in critical dimension measurements in integrated circuit development.

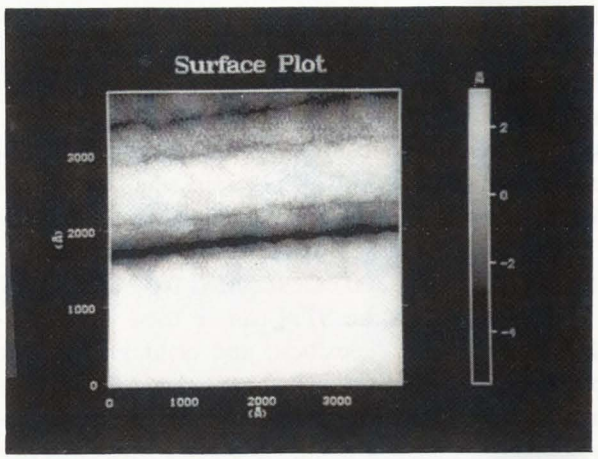

Figure 18. STM image of a magnetic storage medium from a hard disk drive. The image shows a formed groove and grains from the thin film on the surface. The scan size is 400x400 nm.

Scanning Force Microscope

One of the most important developments since the STM is the atomic force microscope (AFM). The AFM was originally introduced by Binnig *et al.* (1986) for measuring surface morphology in the atomic repulsion mode. Generally, the force microscope can be used to study several different probe-surface interactions. These interactions include interatomic, frictional, magnetic, electrostatic, and adhesion forces. The force microscope is also used as a high resolution imaging device for both conductive and insulating materials, significantly adding to the capabilities of the STM. Because of the different applications of the force microscope, we will refer to it as the scanning force microscope (SFM). A complete review of the SFM and its applications is given by Sarid (1991).

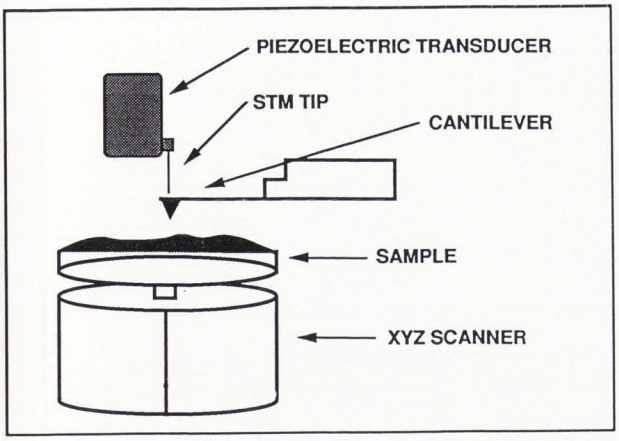

Figure 19. Schematic representation of the tunneling detection method for the SFM. The tip is brought into tunneling on the back of the cantilever. As the sample is scanned under the cantilever, the deflection of the cantilever is sensed from a change in tunneling current. A signal is sent out to correct the position of the sample and therefore the cantilever.

Principles of Operation

The principle of operation of the force microscope is similar to other stylus profilometers except the forces and deflections in the SFM are much smaller (10^{-8} to 10^{-11} N) than those of conventional stylus profilometers (10^{-3} to 10^{-6} N). A sharp point is mounted on a flexible cantilever and is moved across the surface. There are three modes of operation. In the constant force mode, the deflection of the cantilever is held constant by adjustment of the vertical position of the tip or the sample with a feedback loop similar to that of the STM. In a second implementation, the sample is kept at a constant height and the deflection of the cantilever is recorded. The deflection of the cantilever is used to reconstruct the surface topography. The last implementation is mostly used to measure the long range forces. In this mode, the cantilever is modulated near its resonance frequency and the amplitude of the vibration is monitored as the tip is brought near the surface.

Most of the instrumentation and mechanical design requirements for the SFM are the same as those for the STM. The only additional requirements are the electronics and mechanical system associated with the technique used to detect the cantilever deflection, which is described below.

Deflection Detection Systems

The first technique used to detect the deflection of the cantilever was based on tunneling between a tip and the back of the cantilever (Binnig *et al.*, 1986). In this implementation, the tip is brought into tunneling range behind the cantilever. As the sample is scanned under the cantilever, its z-position is adjusted in response to the change in tip-cantilever tunnel current. A feedback loop similar to that of the STM is used to control the sample position. This is schematically represented in Figure 19. Although this technique has the inherent high vertical resolution of STM, it has many disadvantages. Since the tunneling tip is only several Ångstroms from the cantilever, it exerts a force on the cantilever. The tip also interacts with the cantilever through the contamination present in air. The tunneling current is sensitive to the roughness of the backside of the cantilever because of the thermal drift in the position of the tip.

Another technique used to measure the deflection of the cantilever is the capacitance method. The capacitance is measured between the back of the cantilever and a capacitance probe (Goddenhenrich *et al.*, 1990). A capacitance probe was originally used to map the lateral dopant profile on silicon (Williams *et al.*, 1990). This approach is prone to thermal drift.

Interferometry has also been used to detect the motion of the cantilever (Figure 20). Martin *et al.* (1987) used an optical heterodyne detection system to measure the motion of the cantilever. In this method, the cantilever is vibrated near its resonance frequency close to the surface. The tip displacement can be measured over a large range of frequencies and amplitudes with high sensitivity. These authors were able to measure the tip-sample force with the tip-sample spacing of 30 to 150 Å. Also, they used the force signal to maintain a constant tip-sample spacing and to image the surface with 50 Å resolution. An improvement to this technique was offered by Hobbs *et al.* (1989) who added a lock-in detection. They used the instrument for magnetic imaging with 25 nm resolution.

A homodyne detection system was used by McClelland *et al.* (1987) to obtain images with a lateral resolution of 20 nm and a vertical resolution of 1 nm. Rugar *et al.* (1988) used a fiber-optic interferometer along with the homodyne detection system. A sensitivity of 1.7×10^{-4} Å / $\sqrt{\text{Hz}}$ was measured above 2 kHz.

A technique developed by Sarid *et al.* (1988) uses interference effects in a laser diode to sense the motion of the cantilever. In this technique, a laser diode with an integral photodetector is mounted on the back of the cantilever. The cantilever is mounted

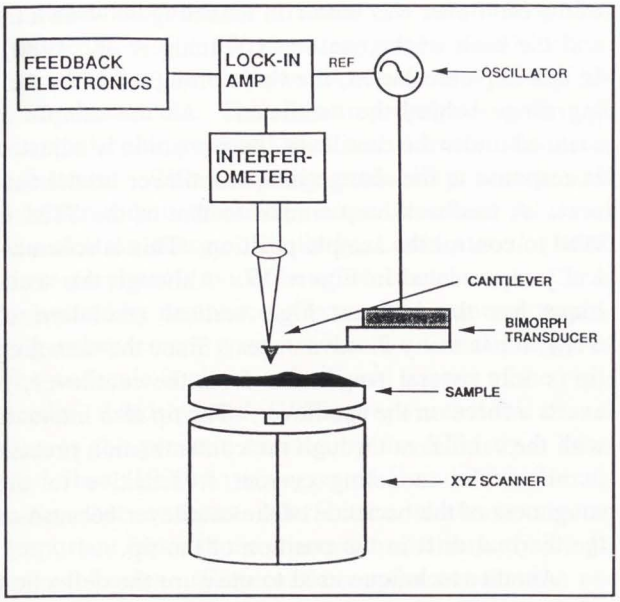

Figure 20. Schematic representation of an interferometer-based deflection sensor.

---

on a piezoelectric ceramic for modulation (Figure 21). The laser light is highly divergent, and only a small amount of the reflected light reenters the laser. This light interferes with the gain medium and a signal is generated at the photodiode. The signal is at the same frequency as that of the modulation frequency of the cantilever and is measured with a lock-in amplifier.

The laser-diode feedback sensor can be made small, as shown in Figure 22(a). The output from a phase sensitive detector connected to the sensor for a 1 Å amplitude vibration of a cantilever is shown in Figure 22(b). The minimum detectable signal was found to be 0.03 Å, which was limited by the thermal vibration of the cantilever. An image of a magnetic domain on a magneto-optic storage medium is shown in Figure 22(c). The image was taken using the laser-diode feedback system (Sarid *et al.*, 1990).

The simplest and most widely used technique is the optical lever method. In this implementation (Meyer and Amer, 1988), a beam from a laser diode is focused on the back of the cantilever. The beam is then deflected into a split photodiode detector. The difference signal from the split photodiode detector is used for feedback control. If the cantilever bends, the beam shifts slightly from one side of the detector to the other side resulting in a change in the difference signal (see Figure 23). The relative position of the cantilever-sample is then adjusted to return the difference signal to the setpoint value.

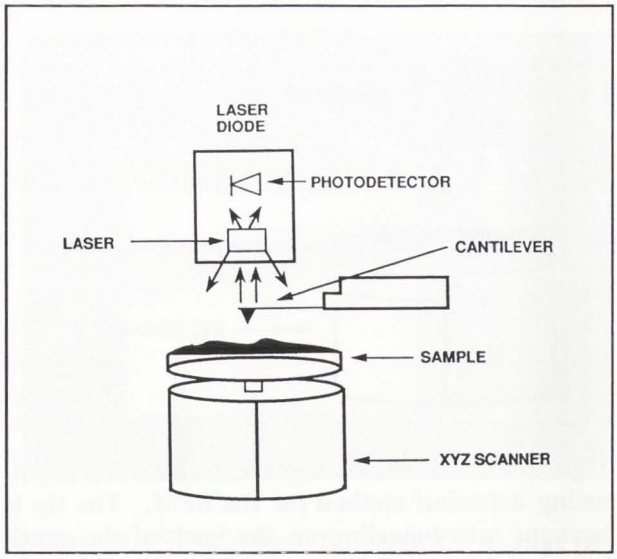

Figure 21. Schematic representation of a laser-diode feedback system. The laser diode is placed behind the cantilever. A small amount of light reflected from the cantilever enters the laser diode and interferes with the gain medium. The change in the output of the laser diode is detected in the integral photodiode. This signal is used to monitor the deflection of the cantilever.

Force Sensors - Cantilevers

Cantilevers play a critical role in force microscopy. For consistent measurements, cantilevers have to be made reproducibly. The cantilevers have to be soft enough to deflect with small forces. Experimental evidence suggests that forces needed for measurements are 10^{-8} to 10^{-11} N. If we assume that the measurement sensitivity for deflection of the cantilevers is 1 Å, then the cantilevers must have force constants of 0.1 to 100 N/m. The force constant for a rectangular cantilever is given by (Vedosic, 1987):

$$k = \frac{Et^3w}{4L^3}$$

where E is the modulus of elasticity, t is the thickness, w is the width, and L is the length. For triangular cantilevers, the force constant can be approximated to that of two rectangular cantilevers in parallel (Albrecht, 1989).

Cantilevers must also have high resonance frequencies to achieve fast imaging. The resonance frequency of a rectangular cantilever is given by (Thompson, 1987):

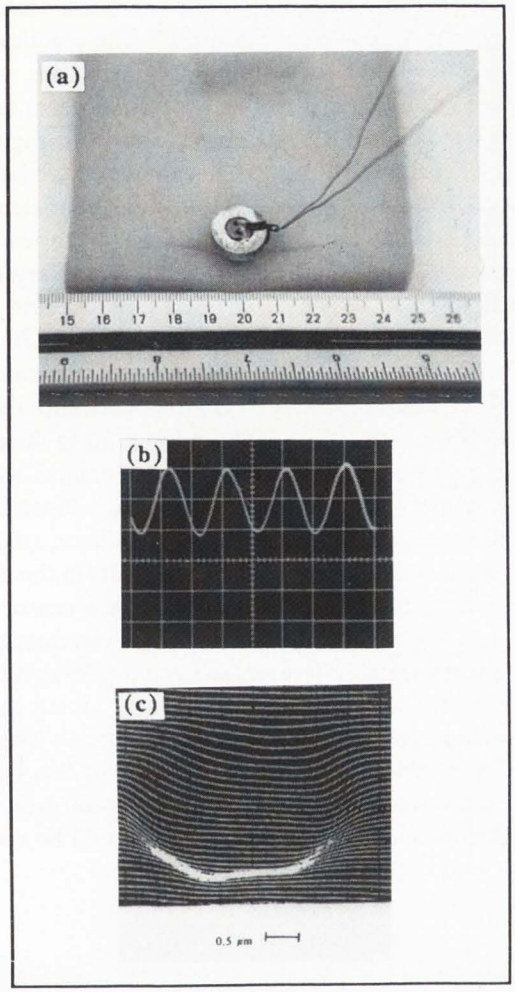

Figure 22. Performance and size of laser-diode feedback system. (a) The actual size of the laser-diode feedback system. (b) The output signal from the phase sensitive detector when the cantilever was vibrated with a 1 Å amplitude. (c) An image of a magnetic domain on a magneto-optic storage medium. The diameter of the domain is 2.5 μm. (Photos courtesy of D. Sarid).

$$F_r = 0.162 \frac{E^{1/2} t}{\rho^{1/2} L^2}$$

where ρ is the density of the material. Typically, the cantilevers should have resonance frequencies which are 100 times higher than the fastest scan rate, 10 to 100 kHz. This is achieved by making cantilevers small. If the cantilever is used in a non-static mode such that it is vibrated at its resonance frequency,

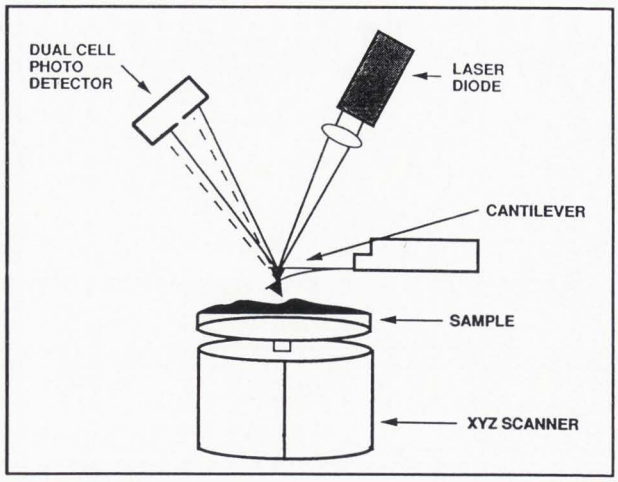

Figure 23. Schematic representation of the optical deflection detection scheme. Light from a laser diode is focused on the back of the cantilever and is reflected into a dual photodiode. As the cantilever bends, the position of the beam on the photodiode changes. The change is reflected in the difference of the output signals from the two halves of the detector. This signal is used in the feedback loop to keep the force on the cantilever constant.

---

then a high mechanical Q will result in higher sensitivity. Cantilevers are made stiff laterally by forming triangular shapes, which results in reduction of the lateral motion during imaging (Albrecht *et al.*, 1990).

The cantilevers used in the initial measurements in force microscopy were either made out of wires or metal foil. The tips were either chemically formed or composed of pieces of diamond that were attached to the foil. Albrecht (1989) has shown that the methods of silicon processing and micromachining can be used to produce cantilevers with integrated tips. The technique for fabrication of Si_3N_4 cantilevers is shown in Figure 24. Using standard processing techniques, a SiO_2 mask is deposited on a Si(100) substrate. Then, 3x3 μm square windows are opened in the mask exposing the silicon substrate. The silicon is anisotropically etched through the windows leaving pyramidal pits. The SiO_2 mask is etched away and a Si_3N_4 film is deposited over the surface conforming to the shape of the pyramidal pits. Cantilever patterns are formed and etched on the Si_3N_4 film. A glass plate (Figure 24c) is anodically bonded to the nitride surface. The Cr coated region of the glass inhibits bonding to the nitride film and is cut away. The silicon substrate is etched away, leaving cantilevers attached to the glass. The back of the cantilever is gold coated to enhance reflection.

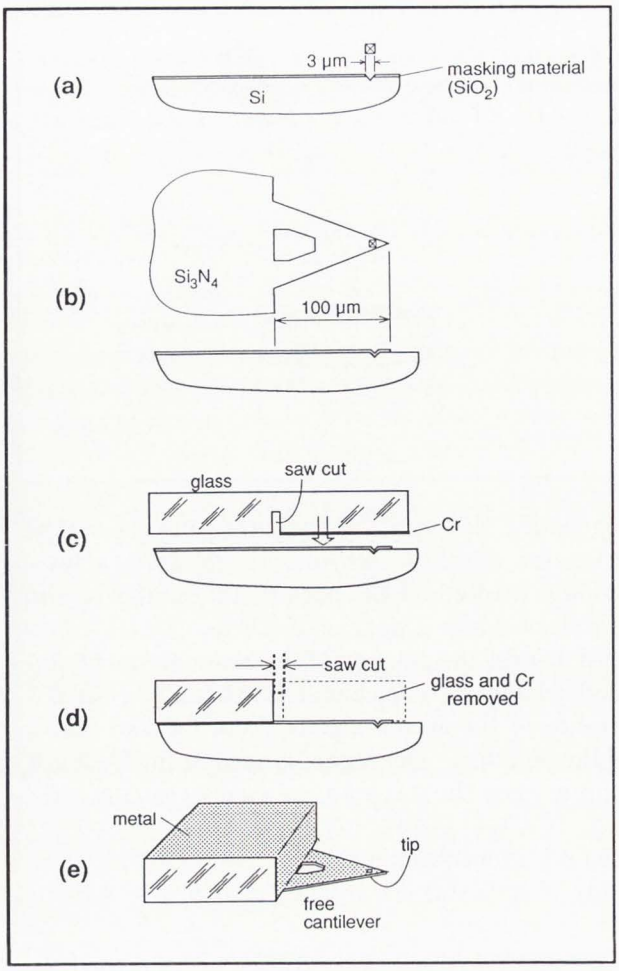

Figure 24. Fabrication of nitride cantilevers with integrated tips. (a) A SiO_2 mask is deposited on a silicon (100) substrate. 3x3 μm windows are opened in the mask and the underlying silicon is anisotropically etched forming pyramidal pits. (b) The silicon mask is removed and a Si_3N_4 film is deposited on the surface which conforms to the shape of the pits. The nitride film is then patterned into the shape of a cantilever. (c) A glass plate is then anodically bonded to the nitride surface. The chrome plating inhibits bonding to the cantilever itself. (d) The glass over the cantilever is sawed off. (e) The underlying silicon is etched leaving the cantilever attached to the glass. The backside of the cantilever is coated for enhanced reflection or conductivity. (Drawings courtesy of T. Albrecht).

Currently, two manufacturers offer cantilever wafers with a large number of cantilever chips and different size cantilevers using fabrication techniques similar to the one described (Park Scientific Instrument and Digital Instruments). An optical image of a cantilever (Park Scientific Instrument's Microlever™) taken on a wafer by Park Scientific Instruments system is shown in Figure 25. The cantilever is 200 μm long and each side is 20 μm wide. An SEM photo showing the side view of a cantilever and the integrated tip near the sample is shown in Figure 26 (PSI Microlever™). Similar techniques have been developed by other research groups for fabricating cantilevers. Akamine *et al.* (1990) have fabricated silicon nitride cantilevers with integral, single-crystal silicon tips. The silicon tip is located at the end of the cantilever and has a radius of curvature of 220 to 400 Å. Wolter *et al.* (1991) have developed cantilevers with integrated sharp, high-aspect-ratio tips. The cantilevers are 100 to 500 μm long, 20 to 40 μm wide, and 4 to 6 μm thick. The tips are conical with a cone angle of less than 40 to 50 degrees. Since the tip, cantilever, and holder are made of silicon single crystal, strains due to thermal mismatch from the deposited thin films are minimized. Also, the sensor is semiconductive and may be used for electrostatic force measurements. Tortonese *et al.* (1991) have fabricated a silicon cantilever with an integrated piezoresistor for sensing the deflection. These authors were able to measure deflections of less than 2 Å. Further development in this area could lead to a very simple and compact SFM which could be used in UHV and at low temperatures.

Applications of SFM

Van der Waals Interaction

When two bodies are brought close to each other, they interact through the Van der Waals forces (in the absence of electrostatic or magnetic forces). The Van der Waals forces are long-range forces and originate from polarization, induction, and dispersion effects (Burnham and Colton, 1992). The polarization force is the result of the interaction of the permanent multipole moments of the molecules. The induction force results from the interaction of the permanent multipole moment of one body with the induced moment of the other. The dispersion force is the result of the induced dipole interaction from the fluctuation of electrons around the nucleus (McClelland *et al.*, 1987).

In general, the major contribution to the van der Waals forces is from dispersion. The interaction potential between two atoms is:

$$U(r) = -C_1/r^6$$

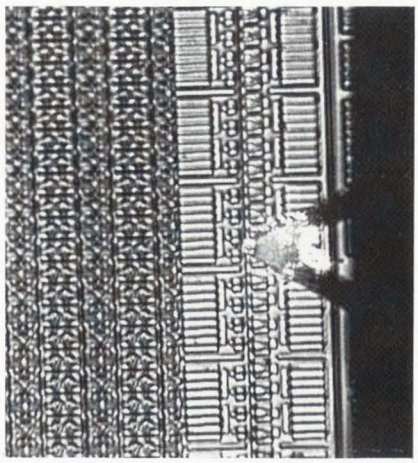

Figure 25. An optical image of a Park Scientific Instruments Microlever™ taken on a wafer. (Photo courtesy of M. Kirk).

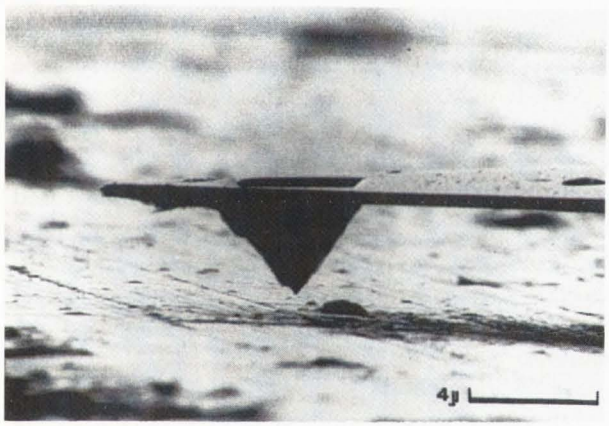

Figure 26. An SEM photograph of a Park Scientific Instruments Microlever™. (Photo courtesy of G. Kelderman).

---

where C_1 is the London dispersion constant and r is the separation distance. For a model of a sphere and a plane, the interaction potential is

$$U(r) = - (AR) / (6r)$$

where A is the Hamaker constant and R is the radius of the sphere. This force can be either attractive or repulsive. The interaction potential for other objects can be found in the book by Israelachvili (1986).

Both attractive and adhesive forces between a cantilever tip and a sample surface have been studied by Burnham *et al.* (1990). These authors used the force microscope to characterize tip-surface interactions as a function of sample surface energy. The SFM was used to observe the surface force difference between samples covered with a monolayer of thin films. The SFM was sensitive enough to distinguish between surface monolayers containing group $-CH_3$ and those containing group $-CF_3$.

An atomistic mechanism for tip-surface interaction has been proposed by Landman *et al.* (1990). They used molecular dynamics simulations to investigate the mechanisms for adhesion, contact formation, nano-indentation, separation and fracture for a nickel tip and a gold surface. Both the theoretical calculations and experimental measurements showed hysteresis in force versus distance curves. Future developments of ultra-high-vacuum based SFMs will allow controlled studies of tip-surface interactions and complete verification of the theoretical findings.

Ionic Repulsion — Atomic Imaging and Topography

As two atoms are brought closer to each other, there is a strong ionic repulsion between them. This ionic repulsion results from the overlapping of the electron clouds around the two atoms. The potential is given by (Lennard-Jones, 1932):

$$U(r) = C_2/r^{12}$$

The topographical images by SFM are usually taken in the repulsive mode. The strong dependence of the force on interatomic spacing allows for atomic resolution imaging with the SFM.

Atomic resolution images have been achieved using the short range repulsive forces. Albrecht and Quate (1987) were the first to obtain atomic resolution images on highly oriented pyrolytic boron nitride, a non-conductor. Binnig *et al.* (1987) used the SFM with the tunneling detection scheme and nitride cantilevers to obtain atomic resolution images of graphite. Atomic resolution images have also been obtained on transition metal dichalcogenides (Albrecht and Quate, 1987; and Meyer *et al.*, 1990), native oxide on silicon (Alexander *et al.*, 1989), lithium flouride (Meyer *et al.*, 1989; and Meyer *et al.*, 1991), and sodium chloride (Meyer and Amer, 1990).

Care must be taken when analyzing atomic resolution images obtained with SFM. To date, all atomic resolution images have been obtained on highly periodic surfaces. Mizes *et al.* (1987), and Albrecht *et al.* (1988) have shown that images with atomic periodicity can be obtained when periodic surfaces are scanned with multiple tips. Abraham and Batra (1989) demonstrated that in order to obtain atomic

resolution with tip forces used in experiments, the effective SFM tip must be composed of several atoms. These authors were able to reproduce a wide variety of images for graphite by assuming that the SFM tip carried a graphite flake while scanning the surface. Atomic resolution images obtained on LiF (a non-layered structure) by Meyer *et al.* (1991) rule out the presence of flakes or shearing of layers as a contrast mechanism. The authors point out that the large force of 10^{-8} N used in their experiments is distributed on the surface by the presence of a contamination layer present on the surface (Mamin *et al.*, 1986). The authors indicated that no decisive interpretation of images could be given due to uncontrolled parameters such as the tip shape, influence of frictional forces (Mate *et al.*, 1987) and presence of adsorbates on the surface. Further progress in interpretation of the atomic resolution images requires a better theoretical understanding of tip-surface interaction and control of the above variables in experiments.

The SFM can be used to image surface morphology from atomic dimensions to over 100x100 μm areas. The surface topography capability allows for imaging of fine details (Figure 27, on color plate at page 639). As integrated circuit technology advances to smaller linewidths, the SFM is expected to become a useful tool for research and development (Figure 28 on color plate at page 639). The SFM instruments can be combined with optical microscopes and used for process control. Future advances in probe technology and encoder based scanners will allow the SFM to be used as a metrology tool for measurements of critical dimensions (Griffith *et al.*, 1992).

Friction

Any two surfaces that are in contact and move relative to each other result in frictional forces. The study of frictional forces and the control of surface wear are important in many technologies ranging from automobile engine components to the sliding regions of magnetic disk media (Miyamoto *et al.*, 1990). Most friction and wear theories are based on macroscopic studies that have been performed and analyzed separately. Miniaturization and micromachining of mechanical parts are making the interacting surfaces smaller. This requires a better understanding of friction on a microscopic scale.

Mate *et al.* (1987) measured the frictional force on a tungsten tip sliding on a graphite substrate for loads $< 10^{-4}$ N. The authors observed that the frictional force displayed a corrugation with periodicity of 2.5 Å with a tip load of 2.4×10^{-5} N. This is the same as the periodicity of the honeycomb structure of the graphite surface. Similar measurements were performed by Erlandsson *et al.* (1988) on a cleaved mica substrate. The frictional force was shown to vary with the periodicity of the hexagonal layer of SiO_4 units that form the cleavage plane of mica.

The force microscope can be used in process control to study and improve wear characteristics of materials. Miyamoto and Kaneko (1991) used a force microscope to study wear marks and frictional force distribution on various thin films. They found that a CF_4 plasma treatment significantly enhances the lubricating effect of the silicon-containing amorphous carbon film.

The above experiments clearly show the dependence of frictional forces on the atomic nature of surfaces and could lead to an understanding of the dynamics of friction on the atomic scale.

Electrostatic Imaging

The SFM is also capable of detecting electrostatic forces. Terris *et al.* (1990) used a force microscope to deposit and image localized charge on the surface. The charge was put on the surface with a 25 ms, 100 V pulse while the tip was 1000 Å away from the surface. As the surface was scanned, the probe sensed the force from the local charge distribution in addition to the van der Waals forces present. The localized charge was distinguished from the topographical features by changing the bias voltage between the cantilever tip and the sample. This also allowed the polarity of the charges to be distinguished.

Similarly, Barrett and Quate (1991b) have used the SFM to store localized charges in nitride-oxide-silicon films. The trapped charge was detected by the change in capacitance between the tip and the sample. The stored charge had an effective size of 750 Å full width at half maximum and was stable over a period of seven days. In a further extension of their work, these authors demonstrated that 256 kilobits of information can be stored over a 120 μm x 120 μm area with an error rate of less than 0.03% (Barrett and Quate, to be published).

Abraham *et al.* (1991) used the force microscope to measure the capacitive forces between the cantilever and the sample. They obtained lateral dopant profiles on silicon from the depletion-induced capacitance. The data were converted into the dopant profile using the known tip geometry. The lateral resolution was limited by the tip diameter and was about 10 to 100 nm. This technique can be used to

measure dopant concentrations from 10^{15} to 10^{20} cm^{-3}. In addition to measuring the dopant profile, the SFM can be used to simultaneously obtain a topographic map of the surface. This is useful in studying devices such as field-effect transistors and p-n junctions in diodes.

Magnetic Media

Magnetic data storage has been moving towards higher density and faster read/write times. For this reason, the read/write head has to move at very high speeds within a few thousand Ångstroms of the surface. This requires stringent conditions on the thin films and the substrates used for the production of magnetic media (Strecker and Persch, 1991).

STM and SFM can be used to monitor and control the surface finish at each process step with high resolution. Bushan and Blackman (1991) used an SFM to investigate the roughness of differently prepared rigid magnetic disks and sliders. They found that the surface topography statistics obtained from the SFM data showed significant differences from the data taken with a non-contact optical profiler. The SFM data showed surface asperities with radii of curvature two to four orders of magnitude smaller than those obtained from the optical profiler data.

The SFM can also be used to measure the distribution of liquid films on surfaces. Thin lubricating films are used on magnetic rigid disks to improve the wear performance. Knowledge of the surface distribution of these films can lead to a better understanding of their lubricating properties. Mate *et al.* (1989) have shown that the thickness of liquid films on surfaces can be measured by using force versus distance curves in an SFM. This is done by moving the sample towards the tip while monitoring the cantilever motion. When the tip comes in contact with the surface, the liquid wicks up around the tip and forms a meniscus which results in an attractive force on the cantilever. As the sample is moved further towards the tip, the force on the cantilever remains constant until tip-substrate contact is made. At this point the force becomes repulsive. The difference in position between the point at which the force becomes attractive and the point where it becomes repulsive is equivalent to the liquid film thickness. This technique was used by Bushan and Blackman (1990) to characterize the distribution of lubricants on magnetic rigid disks. They found a large variation in liquid film thickness across the disk. The average thickness measured was an order of magnitude lower than the nominal value. This result was in agreement with the expectation that a large percentage of the lubricant was in pores below the surface. Mate *et al.* (1989) also mapped the distribution of a liquid film on a substrate by first measuring the liquid surface with the SFM in attractive mode. The image was then subtracted from the image of the substrate obtained with the SFM in repulsive mode. The difference in these images was presented as the liquid film distribution on the surface.

Magnetic heads are also becoming smaller and more sophisticated. Recently, thin film processing has been used to produce pole tips in the magnetic heads. The material used for pole tips is softer than the surrounding area. During mechanical polishing, the pole tip often recesses from the surrounding area and is farther away from the air bearing surface and the magnetic media. Since the signal-to-noise ratio is inversely proportional to the pole tip-magnetic media distance, the control of the pole tip recession is critical. The SFM is used to characterize these pole tips for process control and uniformity with high resolution.

The SFM can also be used to map the magnetic domains of the media with high resolution (Rugar *et al.*, 1988). By using a magnetic cantilever, the microscope can directly sense the magnetic forces. In this implementation, the instrument is referred to as the magnetic force microscope (MFM). The cantilevers used for MFM can either be made directly from ferromagnetic wires or foils, or batch processed cantilevers can be coated with thin ferromagnetic films (Grüther *et al.*, 1990). These authors used the MFM to image 8 μm wide tracks on a longitudinal recording sample using cantilevers with tips magnetized in a different direction relative to the sample. Both attractive and repulsive magnetic interactions were imaged. The MFM image of 5 μm bits on cobalt alloy disk is shown in Figure 29 (Rugar *et al.*, 1990). Figure 30 shows two tracks written at two different frequencies on a previously erased area of Co-alloy disk (Rugar *et al.*, 1990). Light shading was used to emphasize the domain boundaries.

The MFM is easily applied to the study of magnetic media without sample preparation and can be used regardless of the properties of the thin film media or coatings. It is expected that both SFM and MFM will play a significant role in the future development of magnetic storage devices.

Biological Materials and Organic Molecules

As with the STM, one of the most exciting applications of the SFM is the imaging of biological

Figure 29. An MFM image of a 5 μm bit track in Co-alloy. (Photo courtesy of H. J. Mamin).

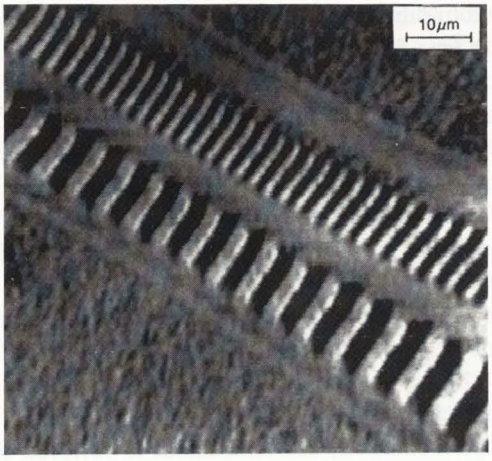

Figure 30. An MFM image of two bit tracks written at two different frequencies on Co-alloy disk. The section of the disk was erased before the bits were written. (Photo courtesy of H. J. Mamin).

---

materials. The SFM can be used to image biological samples in buffer solutions and at room temperature with molecular resolution.

Weisenhorn *et al.* (1990) imaged lipid protein membranes and actin filaments by atomic force microscopy. The proteins were immobilized on lipid membranes on quartz and mica and were submerged in buffer solution. The images obtained depended on the applied force. At a low applied force of less than 5 nN, the authors observed long elevated structures. Submolecular details were visible in the areas packed with proteins. The structures possessed a characteristic four-leaf shape with dimensions of 12x6x2 nm^3 which was correlated to immunoglobulin domains of the proteolipid. The observed sizes were approximately 30% larger than expected because of the tip/sample interaction and the convolution of the tip and sample. With forces above 10 nN, only the underlying membrane was visible. This force was large enough to push the proteins aside. The authors also imaged actin filaments on cleaved mica. The filaments were formed by surface-indu ced polymerization and immobilized by Coulomb interaction to the substrate. The SFM images (with force < 5 nN) showed individual filaments. It was found that forces above 30 nN pushed aside the filaments such that the underlying mica could be imaged.

Single-stranded DNA was imaged by Weisenhorn *et al.* (1991). A 16-mer single stranded DNA containing pyrimidines was immobilized on Langmuir-Blodgett (LB) films. The SFM images of the surface resolved rows of DNA 0.8 to 1.2 nm apart. These authors could not obtain reproducible images with high resolution to sequence the DNA. This was attributed to the non-rigidity of the lipid-DNA covalent attachment and the movement of the DNA under applied force of the cantilever.

The SFM can also be used to image large biological cells. Figure 31 (on color plate at page 640) shows an image taken of blood cells. The blood sample was simply placed on a glass slide and air dried for about half an hour before being imaged. Gould *et al.* (1990) have obtained images of purple membrane dried both on glass and mica substrates. SFM images of the samples are shown in Figures 32(a) and (b). The individual membranes are about 0.5 to 1 μm across and 5 nm high. Magnified images of the samples are shown in Figures 32(c) and (d). The magnified images show periodic order on the membrane. The sample on the glass (Figure 32c) shows periodic order in two directions. The observed periodicity is higher than those obtained with other techniques. This discrepancy was related to either the dullness of the tip and/or the difference between the surface (measured by SFM) and bulk structures (measured with other techniques).

Butt *et al.* (1991) compared the SFM images of purple membranes both air dried and in buffered solution. They found that the slow air-dried purple membranes show cracks. They could not obtain molecular resolution images on these samples. In contrast, the purple membranes imaged in buffer solution on a mica substrate did not have any cracks and the hexagonal packing of the bacteriorhodopsin molecules were resolved.

Figure 33 shows an SFM image of *E. coli* bacteria (Gould *et al.*, 1990). The samples were simply dried onto a glass slide without any other preparations or coatings. The magnified images of the upper and lower bacterium are shown in Figures 33 (b) and 33 (c), respectively.

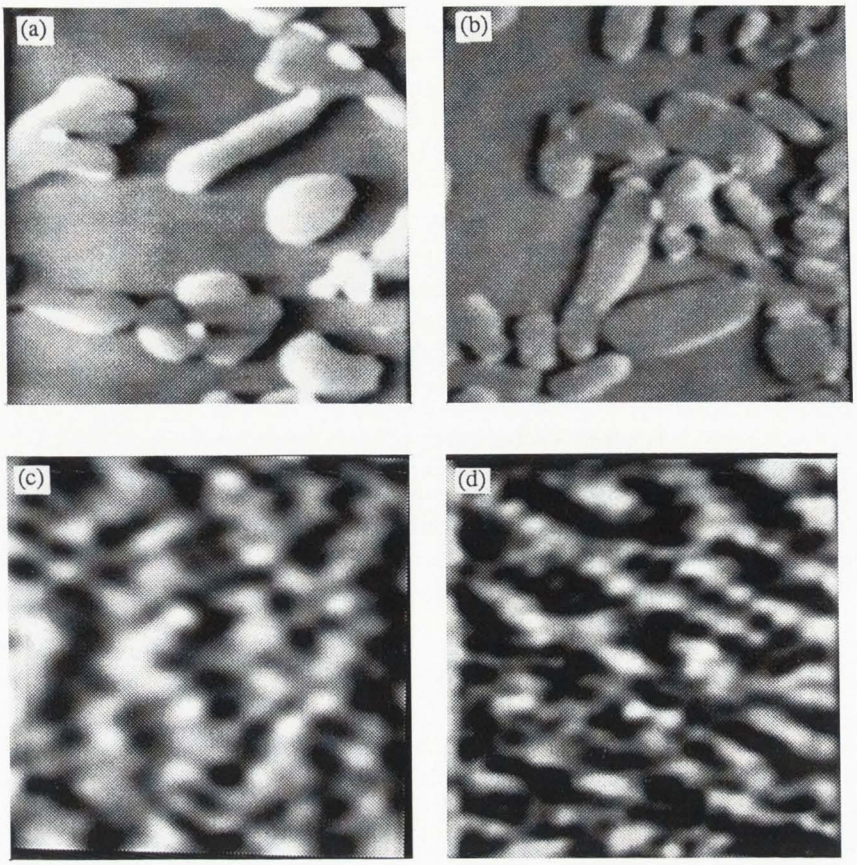

Figure 32 (at right). SFM images of purple membrane (a) deposited on poly-L-lysine coated glass, and (b) sprayed on mica. The scan sizes are 6.2 μm x 6.2 μm. (c) A magnified image of the sample in (a). The scan size is 43 nm. Two sets of diagonal rows can be observed. These correlate with the hexagonal order of the purple membrane. (d) A magnified image of the sample in (b). The scan size is 125 nm.

Figure 33 (below). (a) An SFM image of bacteria E. *coli* which was dried on a glass substrate. The scan size is 9 μm. (b) A magnified image of the upper bacterium. (c) A magnified image of the lower bacterium. The scan size is 1.75 μm for images in (b) and (c).

(Figures 32 and 33 courtesy of P. Hansma and G. Kelderman).

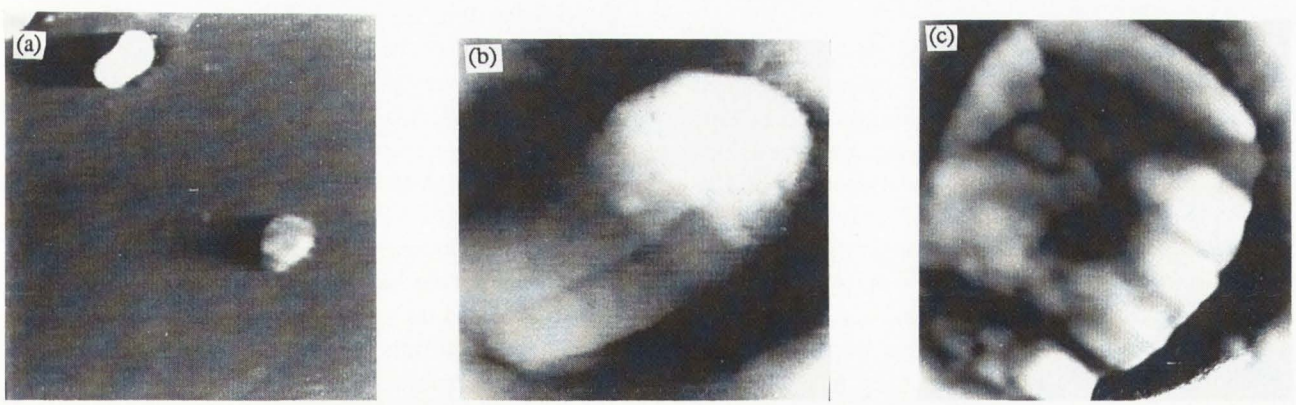

Recently, the SFM was used to image live cells in their natural environments (Haberle *et al.*, 1991). The authors used an underwater atomic force microscope for investigation of living cells. The cells were sucked onto a micropipette and brought into contact with the cantilever for imaging. The manipulations were observed and controlled with an integral optical microscope. They measured images of red blood cells with 100 Å resolution. They also observed changes in the cell membrane, which were induced by increasing the salt concentration of the solution and by adding antibodies to the solution.

Weinsenhorn *et al.* (1990) studied the adsorption of molecules and ions on zeolites using a medium of diluted *tert*-butyl ammonium chloride solution and *tert*-butonal. The solution was introduced through a sealed liquid cell. The SFM images showed that *tert*-butonal formed an ordered monolayer array on the surface. On the other hand, the *tert*-butyl ammonium cations formed clusters that were 2x3x0.6 nm^3. The

clusters took one minute to form and were imaged in real time by the SFM. The clusters could be rinsed with water and then formed again. The authors were also able to rearrange the *tert*-butyl ammonium cations by increasing the force exerted by the tip.

The above results show that SFM can easily be applied to the study of biological materials and organic molecules. The SFM has a great potential in studying the dynamical processes of living cells with nanometer resolution. Future developments in immobilization techniques and preparation of sharper tips may lead to the application of SFM in sequencing DNA.

Related Techniques

The success of the STM has resulted in development of many instruments based on similar technology. The most important of these instruments was the SFM which was discussed in the previous sections.

Near Field Optical Microscopy

A light beam impinging on a sample will diffract as a propagating homogeneous field (far field) and as an evanescent field (near field) that is confined near the sample. It is well known that the spatial resolution of an image formed in far field optics is limited by the wavelength of light used. To improve the resolution, measurements can be made in the near field. This is the basis for the scanning near field optical microscope (SNOM) and scanning photon tunneling microscope (SPTM).

In SNOM (Betzig *et al.*, 1988; and Pohl *et al.*, 1988), a micropipette with a sharp point and a small aperture is used as a light source (illumination mode). The radiation transmitted through the aperture is initially collimated to the size of the aperture and is independent of the wavelength of light. When the micropipette is brought close (near field) to the surface, the light from the aperture is transmitted through the semi-transparent sample and is collected as the sample is scanned. In another implementation (collection mode) the aperture is used to collect the light that is transmitted through the sample (Betzig *et al.*, 1987). A higher resolution is obtained in this mode since the light is collected in the near field. SNOM can also be operated in the reflection mode (Fischer, 1990) where the aperture is used for illumination and collection of light. Currently, the resolution of SNOM is a few hundred Ångstroms and is limited by difficulties in forming reproducible subwavelength apertures. Applications include imaging of biological materials and mapping the luminescence of surfaces and thin films.

In SPTM (Reddick *et al.*, 1989), a sharpened optical probe tip is brought close to the surface in the evanescent field. The photons are transmitted through the optical fiber to a photomultiplier tube to produce electrical currents. The current is then used in a feedback loop, similar to the STM, to keep the tip near the surface as it is scanned in the x and y directions. The evanescent field is produced by mounting the sample on a prism and directing the light to the back of the sample such that it is internally reflected. Because of the exponential decay of the evanescent field with distance, the resolution normal to the sample is about 1 nm (Ferrell *et al.*, 1991). The lateral resolution is not wavelength limited and depends on the size of the stylus. A lateral resolution of 20 nm ($\lambda/12$) has been obtained by Courjon (1990). The potential applications of SPTM are imaging biological samples and metrology.

Ballistic Energy Electron Microscopy

Interfaces of thin films are of major interest to thin film scientists and device physicists. The interfaces are not easily accessible and require destructive or indirect evaluation. An extension of STM called ballistic energy electron microscopy (BEEM) was developed by Kaiser and Bell (1988). The technique allows nondestructive evaluation of Schottky barriers at the interface of thin films ($<$ 100 Å thick) (Bell and Kaiser, 1988). The method involves three electrodes, the tip, the thin film, and the substrate. The tip is brought into tunneling near the thin film as in a normal STM. Since the mean free path of the low energy tunneling electrons is greater than 100 Å, some travel to the interface. If the energy of these electrons is less than the barrier height at the interface, they are reflected. As the energy of the electrons is increased by increasing the tip voltage, some will cross the interface barrier and will be collected at the substrate electrode. This current is used to map the interfacial electronic properties in addition to the surface topographical features.

Fernandez *et al.* (1991) used BEEM to study the $NiSi_2$/Si(111) interface. Two orientations of $NiSi_2$ can be grown on Si(111): type A and B. In type A, the silicide has the same orientation as the substrate. In type B, the silicide is rotated 180 degrees about the (111) direction. The authors measured the Schottky barrier heights of these interfaces and found them to be in close agreement with previous studies.

A powerful demonstration of the capabilities of BEEM was performed by Hallen *et al.* (1991). The authors modified the interface of Au-Si by ballistic

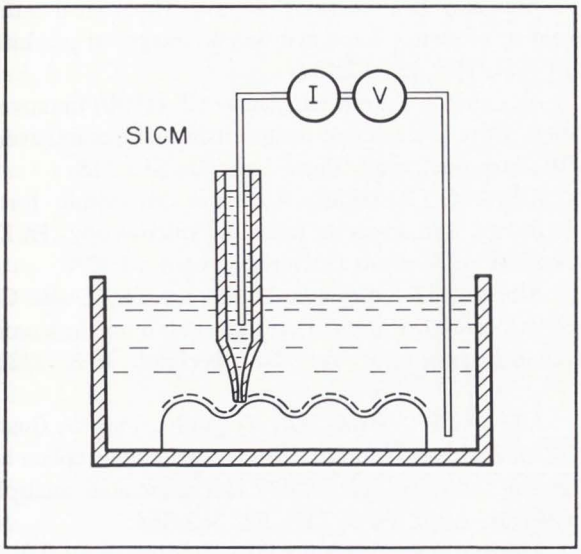

Figure 34. Schematic representation of the scanning ion conductance microscope. (Drawing courtesy of P. Hansma and G. Kelderman).

---

electrons. The modified area was then imaged with BEEM and compared with the surface topography. They found that the modification consisted of a region, a few hundred Ångstroms in diameter, with decreased ballistic transmittance. This region was surrounded by a ring which had higher ballistic transmittance. They correlate the decrease in current to the interdiffusion of Au-Si and the increase in current to modification of the interface impurity layer.

Scanning Thermal Profiler

The scanning thermal profiler (Williams and Wickramasinghe, 1986) uses a heated sensor consisting of a thermocouple junction with approximate dimensions of 100 nm. As the heated tip is brought close to the surface, the temperature of the tip is reduced because of thermal coupling between the tip and the sample. Therefore, the temperature of the tip is a function of the gap spacing. During the measurement of surface profile, the temperature of the tip is varied sinusoidally. The detected ac temperature of the tip is used in the servo control loop similar to that of the STM. The probe is then scanned over the surface to obtain a three-dimensional profile. The technique has a lateral resolution of 100 nm and a vertical resolution of 3 nm independent of the surface being probed. The profiler can be used with gap spacings of $>$ 10 nm which makes it useful for non-contact profiling of non-conductive materials.

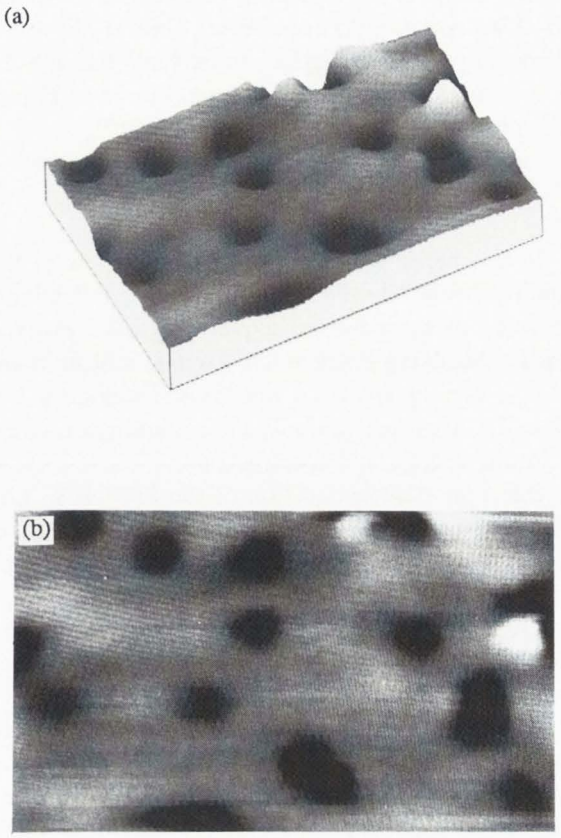

Figure 35. (a) An image of a Nuclepore membrane filter taken with the scanning ion-conductance microscope. The pores are 0.8 μm in diameter. The scan size is 7.8 x 4.5 μm for all three images. (b) Top view of the image in (a). (c, shown on color plate at page 640) The image of ion currents from the pores taken with the scanning ion-conductance microscope. (Photos courtesy of P. Hansma and G. Kelderman).

Scanning Ion-Conductance Microscope

The scanning ion-conductance microscope (SICM) is based on the flow of ions through a micropipette (Hansma *et al.*, 1989). The micropipette is placed in an electrolyte solution and is scanned near the sample (see Figure 34). As the pipette gets closer to the surface, the flow of ions is blocked and the current decreases. When the pipette moves away from the surface, the ion current increases. The flow of the current through the micropipette is used to control its position near the surface, similar to STM. The SICM can be used to measure both topography and local ion currents near the surface. The topo-

graphic image of a Nuclepore (Nuclepore Corporation, Pleasanton, CA) membrane filter is shown in Figures 35(a) and (b). The ion currents through the 0.8 μm pores of the same filter are shown in Figure 35(c, presented on color plate at page 640).

Conclusions

In this paper we have presented a review of the scanning probe microscope, its many applications, and some of the new techniques that have evolved from it. Scanning probe microscopy is still in its infancy. The applications and new techniques described in this paper are only the beginning of a new era in microscopy and spectroscopy.

One important application of the SPM is in metrology. The development of sub-micron features on integrated circuits is currently pushing the limits of optical metrology. It is expected that further development in probes, ease of use, and automation of the SPM will allow its use in manufacturing and process control environments.

Perhaps the most exciting potential use of the SPM is the imaging of complex biomolecules. The atomic force microscope offers advantages in size, cost, and sample preparation over scanning electron and transmission electron microscopes. Potential applications of the microscope include cell biology and medical research. Advances in genetic research are sure to follow the ability to image and identify complex biological systems.

Acknowledgments

We would like to thank W. Conley, M. Courtney, E. Frey, and J. Muller for their assistance in measurements. We thank T. Albrecht, D.M. Eigler, R. M. Feenstra, J.E. Griffith, P. Hansma, G. Kelderman, M. Kirk, H.J. Mamin, C.R.K. Marrian, L. Rapp, and D. Sarid for providing us with the photographs of their work. We thank K. Snail and C. Marks for the diamond sample. Also, we would like to thank K. Seeley for editing and putting this manuscript in its final form.

References

Abraham DW, Mamin HJ, Ganz E, Clarke J (1986) Surface modification with the STM. IBM J. Res. Develop. **30**, 492-499.

Abraham DW, Williams C, Slinkman J, Wickramasinghe HK (1991) Lateral dopant profiling in semiconductors by force microscopy using capacitive detection. J. Vac. Sci. Technol. **B 9**, 703-706.

Abraham FF, Batra IP (1989) Theoretical interpretation of atomic force microscope images of graphite. Surf. Sci. **209**, L125-L132.

Akamine S, Barrett RC, Quate CF (1990) Improved atomic force microscope images using microcantilevers with sharp tips. Appl. Phys. Lett. **57**, 316-318.

Albrecht TR (1989) Advances in atomic force microscopy and scanning tunneling microscopy. Ph.D. Dissertation, Stanford University, Stanford, CA.

Albrecht TR, Akamine S, Carver TE, Quate CF (1990) Microfabrication of cantilever styli for the atomic force microscope. J. Vac. Sci. Technol. **A 8**, 3386-3396.

Albrecht TR, Mizes HA, Nogami J, Park S, Quate CF (1988) Observation of tilt boundaries in graphite by scanning tunneling microscopy and associated multiple tip effects. Appl. Phys. Lett. **52**, 362-364.

Albrecht TR, Quate CF (1987) Atomic resolution imaging of nonconductors by atomic force microscopy. J. Appl. Phys. **62**, 2599-2602.

Alexander S, Hellemans L, Marti O, Schneir J, Elings V, Hansma PK (1989) An atomic-resolution atomic-force microscope implemented using an optical lever. J. Appl. Phys. **65**, 164-167.

Amrein M, Stasiak A, Gross H, Stoll E, Travaglini G (1988) Scanning tunneling microscopy of recA-DNA complexes coated with a conducting film. Science **240**, 514-516.

Amrein M, Wang Z, Guckenberger R (1991) Comparative study of a regular protein layer by scanning tunneling microscopy and transmission electron microscopy. J. Vac. Sci. Technol. **B 9**, 1276-1281.

Arscott PG, Lee G, Bloomfield VA, Evans DF (1989) Scanning tunneling microscopy of Z-DNA. Nature **339**, 484-486.

Avouris Ph, Lyo I-W, Bozso F, Kaxiras E (1990) Adsorption of boron on Si(111): Physics, chemistry, and atomic-scale electronic devices. J. Vac. Sci. Technol. **A 8**, 3405-3411.

Bard AJ, Fran FRF, Kwak J, Lev O (1989) Scanning electrochemical microscopy. Introduction and principles. Anal. Chem. **61**, 132-138.

Bardeen J (1961) Tunnelling from a many-particle point of view. Phys. Rev. Lett. **6**, 57-59.

Barrett RC, Quate CF (1991a) Optical scan-correction system applied to atomic force microscopy. Rev. Sci. Instrum. **62**, 1393-1399.

Barrett RC, Quate CF (1991b) Charge storage in a nitride-oxide-silicon medium by scanning capacitance microscopy. J. Appl. Phys. **70**, 2725-2733.

Barrett RC, Quate CF (1992) Large-scale charge storage by scanning capacitance microscopy. Ultramicroscopy, in press.

Barris B, Knipping U, Lindsay SM, Nagahara L,

Thundat T (1988) Images of DNA fragments in an aqueous environment by scanning tunneling microscope. Biopolymers **27**, 1691-1696.

Becker RS, Golovchenko JA, Swartzentruber BS (1985a) Tunneling images of 5x5 surface reconstruction on Ge-Si(111). Phys. Rev. **B 32**, 8455-8457.

Becker RS, Golvchenko JA, Swartzentruber BS (1985b) Tunneling images of germanium surface reconstructions and phase boundaries. Phys. Rev. Lett. **54**, 2678-2680.

Beebe Jr. TP, Wilson TE, Ogletree DF, Katz JE, Balhorn R, Salmeron MB, Siekhaus WJ (1989) Direct observation on native DNA structures with the scanning tunneling microscope. Science **243**, 370-372.

Behm RJ, Hosler W, Ritter W, Binnig G (1986) Correlation between domain boundaries and surface steps: A STM study on reconstructed Pt(100). Phys. Rev. Lett. **56**, 228-231.

Bell LD, Kaiser WJ (1988) Spatially resolved ballistic electron spectroscopy of subsurface interfaces. J. Microscopy **152**, 605-610.

Besocke K (1987) An easily operable scanning tunneling microscope. Surf. Sci. **181**, 145-153.

Betzig E, Isaacson M, Barshatzky H, Lewis A, Lin K (1988) Near field scanning optical microscopy (NSOM). Proc. SPIE **897**, 91-99.

Betzig E, Isaacson M, Lewis A (1987) Collection mode near field scanning optical microscopy. Appl. Phys. Lett. **51**, 2088-2090.

Biegelsen DK, Ponce FA, Tramontana JC, Koch SM (1987) Ion milled tips for scanning tunneling microscopy. Appl. Phys. Lett. **50**, 696-698.

Binh VT (1988) In situ fabrication and regeneration of microtips for scanning tunneling microscopy. J. Microscopy **152**, 355-361.

Binnig G, Gerber Ch, Stoll E, Albrecht TR, Quate CF (1987) Atomic resolution with atomic force microscope. Europhys. Lett. **3**, 1281-1286.

Binnig G, Quate CF, Gerber Ch (1986) Atomic force microscope. Phys. Rev. Lett. **56**, 930-933.

Binnig G, Rohrer H (1982) Scanning tunneling microscope. Helv. Phys. Acta **55**, 726-735.

Binnig G, Rohrer H, Gerber Ch, Stoll E (1984) Real-space observation of the reconstruction of Au(100). Surf. Sci. **144**, 321-335.

Binnig G, Rohrer H, Gerber Ch, Weibel E (1982) Tunneling through a controllable vacuum gap. Appl. Phys. Lett. **40**, 178-180.

Binnig G, Rohrer H, Gerber Ch, Weibel E (1983a) 7x7 reconstruction on Si(111) resolved in real space. Phys. Rev. Lett. **50**, 120-123.

Binnig G, Rohrer H, Gerber Ch, Weibel E (1983b) (111) Facets as the origin of reconstructed Au(110) surface. Surf. Sci. **131**, L379-L384.

Binnig G, Smith DPE (1986) Single-tube three-dimensional scanner for scanning tunneling microscopy. Rev. Sci. Instrum. **57**, 1688-1689.

Blackford BL, Jericho MH, Mulhern PJ, Frame C, Southam G, Beveridge TJ (1991) Scanning tunneling microscope imaging of hoops from cell sheath of the bacteria methanospirillum hungatei and atomic force microscope imaging of complete sheathes. J. Vac. Sci. Technol. **B 9**, 1242-1247.

Burnham NA, Colton RJ (1992) Force microscopy. In: *Scanning Tunneling Microscopy: Theory and Application.* Bonnell D (ed.) VCH Publishers, to be published.

Burnham NA, Dominguez DD, Mowery RL, Colton RJ (1990) Probing the surface forces of monolayer films with an atomic-force microscope. Phys. Rev. Lett. **64**, 1931-1934.

Bushan B, Blackman GS (1991) Atomic force microscopy of magnetic rigid disks and sliders and its application to tribology. J. Tribology **113**, 452-457.

Butt H-J, Prater CB, Hansma PK (1991) Imaging purple membranes dry and in water with the atomic force microscope. J. Vac. Sci. Technol. **B 9**, 1193-1196.

Carr RG (1988) Finite element analysis of PZT tube scanner motion for scanning tunneling microscopy. J. Microscopy **152**, 379-385.

Chang H, Bard AJ (1991) Observation and characterization by scanning tunneling microscopy of structures generated by cleaving highly oriented pyrolytic graphite. Langmuir **7**, 1143-1153.

Chiang S, Wilson RJ (1986) Construction of a UHV STM. IBM J. Res. Develop. **30**, 515-519.

Clemmer CR, Beebe Jr. TP (1991) Graphite: A mimic for DNA and other biomolecules in scanning tunneling microscope studies. Science **251**, 640-642.

Colton RJ, Baker SM, Baldeschwieler JD, Kaiser WJ (1987) Oxide-free tip for scanning tunneling microscopy. Appl. Phys. Lett. **51**, 305-307.

Courjon D (1990) Scanning tunneling optical microscopy. In: *Scanning Tunneling Microscopy and Related Methods,* Behm RJ, Garcia N, Rohrer R (eds.), NATO ASI series, Series E, vol. 184, Kluwer Academic Publishers, Boston, 497-505.

Craston DH, Lin CW, Bard AJ (1988) High resolution deposition of silver in nafion films with the scanning tunneling microscope. J. Electrochem. Soc. **135**, 785-786.

Dagata JA, Schneir J, Harary HH, Bennett J, Tseng W (1991) Pattern generation on semiconductor surfaces by a scanning tunneling microscope operating in air. J. Vac. Sci. Technol. **B 9**, 1384-1388.

de Lozanne AL, Elrod SA, Quate CF (1985) Spatial variations in the superconductivity of Nb_3Sn measured

by low-temperature tunneling microscopy. Phys. Rev. Lett. **54**, 2433-2436.

Demuth JE, Hamers RJ, Tromp R, Welland ME (1986) A simplified STM for surface science studies. J. Vac. Sci. Technol. **A 4**, 1320-1323.

Dobisz EA, Marrian CRK (1991) Sub-30nm lithography in a negative electron beam resist with a vacuum scanning tunneling microscope. Appl. Phys. Lett. **58**, 2526-2528.

Dragoset RA, Young RD, Layer HP, Mielczarek SR, Teague EC, Celotta RJ (1986) Scanning tunneling microscopy applied to optical surfaces. Optics Letters **11**, 560-562.

Driscoll RJ, Youngquist MG, Baldeschwieler JD (1990) Atomic-scale imaging of DNA using scanning tunnelling microscopy. Nature **346**, 294-296.

Dunlap DD, Bustamante C (1989) Images of single-stranded nucleic acids by scanning tunneling microscopy. Nature **342**, 204-206.

Edstrom RD, Meinke MH, Yang X, Yang R, Evans DF (1989) Direct observation of phosphorylase kinase and phosphorylase b by scanning tunneling microscopy. Biochem. **28**, 4939-4942.

Edstrom RD, Miller MA, Elings VB, Yang X, Yang R, Lee G, Evans DF (1991) Scanning tunneling microscopy and atomic force microscopy visualization of the components of the skeletal muscle glycogenolytic complex. J. Vac. Sci. Technol. **B 9**, 1248-1252.

Ehrichs EE, Silver RM, de Lozanne AL (1988) Direct writing with the scanning tunneling microscope. J. Vac. Sci. Technol. **A 6**, 540-543.

Eigler DM, Schweizer EK (1990) Positioning single atoms with a scanning tunnelling microscope. Nature **344**, 524-526.

Elrod SA, Bryant A, de Lozanne AL, Park S, Smith D, Quate CF (1986) Tunneling microscopy from 300 to 4.2 K. IBM J. Res. Develop. **30**, 387-395.

Erlandsson R, Hadziioanou G, Mate CM, McClelland GM, Chiang S (1988) Atomic scale friction between the muscovite mica cleavage plane and a tungsten tip, J. Chem. Phys. **89**, 5190-5193.

Feenstra RM (1990) Scanning tunneling microscopy: Semiconductor surfaces, adsorption, and epitaxy. In: *Scanning Tunneling Microscopy and Related Methods*, Behm RJ, Garcia N, Rohrer R (eds.), NATO ASI series, Series E, vol. 184, Kluwer Academic Publishers, Boston, 211-263.

Feenstra RM, Fein AP (1985) Surface morphology of GaAs(110) by STM. Phys. Rev. **B 32**, 1394-1396.

Feenstra RM, Slavin AF (1991) Scanning tunneling microscopy and spectroscopy of cleaved and annealed Ge(111) surfaces. Surf. Sci. **251/252**, 401-407.

Feenstra RM, Stroscio JA (1987) Tunneling spectroscopy of the GaAs(110) surface. J. Vac. Sci. Technol. **B 5**, 923-929.

Feenstra RM, Stroscio JA, Tersoff J, Fein AP (1987) Atom-selective imaging of the GaAs(110) surface. Phys. Rev. Lett. **58**, 1192-1195.

Fernandez A, Hallen HD, Huang T, Buhrman RA, Silcox J (1991) Ballistic electron emission microscopy studies of the $NiSi_2$/Si(111) interface. J. Vac. Sci. Technol. **B 9**, 590-593.

Ferrell TL, Goudonnet JP, Reddick RC, Sharp SL, Warmack RJ (1991) The photon scanning tunneling microscope. J. Vac. Sci. Technol. **B 9**, 525-530.

Feuchtwanga TE, Cutler PH (1987) Tunneling and scanning tunnel microscopy. Phys. Scr. **35**, 132-140.

Fischer UCh, (1990) Resolution and contrast generation in scanning near field optical microscopy. In: *Scanning Tunneling Microscopy and Related Methods*, Behm RJ, Garcia N, Rohrer R (eds.), NATO ASI series, Series E, vol. 184, Kluwer Academic Publishers, Boston, 475-496.

Gehrtz M, Strecker H, Grimm H (1988) Scanning tunneling microscopy of machined surfaces. J. Vac. Sci. Technol. **A 6**, 432-435.

Gerber Ch, Binnig G, Fuchs H, Marti O, Rohrer H (1986) STM combined with a scanning electron microscope. Rev. Sci. Instrum. **57**, 221-224.

Gewirth AA, Craston DH, Bard AJ (1989) Fabrication and characterization of microtips for *in situ* scanning tunneling microscopy. J. Electroanal. Chem. **261**, 477-482.

Goddenhenrich T, Lemke H, Hartmann U, Heiden C (1990) Force microscope with capacitive displacement detection. J. Vac. Sci. Technol. **A 8**, 383-387.

Gould SAC, Drake B, Prater CB, Weisenhorn AL, Manne S, Hansma HG, Massie J, Longmire A, Elings V, Dixon Northern B, Mukergee B, Peterson CM, Stoeckenius W, Albrecht TR, Quate CF (1990) From atoms to integrated circuit chips, blood cells, and bacteria with the atomic force microscope. J. Vac. Sci. Technol. **A 8**, 369-373.

Green MP, Richter M, Xing X, Scherson D, Hanson KJ, Ross Jr. PN, Carr R, Lindau I (1988) *In-situ* STM studies of electrochemical underpotential deposition of Pb on Au(111). J. Microscopy **152**, 823-829.

Griffith JE, Grigg DA, Vasile MJ, Russell PE, Fitzgerald EA (1991) Characterization of scanning probe microscope tips for linewidth measurement. J. Vac. Sci. Technol. **B 9**, 3586-3589.

Griffith JE, Grigg DA, Vasile MJ, Russell PE, Fitzgerald EA (1992) Scanning probe metrology. J. Vac. Sci. Technol. A, in press.

Griffith JE, Kochanski GP (1990) The atomic structure of vicinal Si(001) and Ge(001). Critical Review in Solid State and Materials **16**, 255-289.

Griffith JE, Miller GL, Green CA, Grigg DA, Russell PE (1990) A scanning tunneling microscope with a capacitance-based position monitor. J. Vac. Sci. Technol. **B 8**, 2023-2027.

Grüther P, Rugar D, Mamin HJ, Castillo J, Lambert SE, Lin C-J, Valleta RM, Wolter O, Bayer T, Greschner J (1990) Batch fabricated sensors for magnetic force microscopy. Appl. Phys. Lett. **57**, 1820-1822.

Haberle W, Horber JKH, Binnig G (1991) Force microscopy on living cells. J. Vac. Sci. Technol. **B 9**, 1210-1213.

Hallen HD, Fernandez A, Huang T, Buhrman RA, Silcox J (1991) Gold-silicon interface modificatio n studies. J. Vac. Sci. Technol. **B 9**, 585-589.

Hansma PK, Drake B, Marti O, Gould SAC, Prater CB (1989) The scanning ion-conductance microscope. Science **243**, 641-643.

Hansma PK, Tersoff J (1986) Scanning tunneling microscope. J. Appl. Phys. **61**, R1-R23.

Heben MJ, Dovek MM, Lewis NS, Penner RM, Quate CF (1988) Preparation of STM tips for *in situ* characterization of electrode surfaces. J. Microscopy **152**, 651-661.

Heben MJ, Penner RM, Lewis NS, Dovek MM, Quate CF (1989) Atomic resolution imaging of electrode surfaces in solutions containing reversible redox species. Appl. Phys. Lett. **54**, 1421-1423.

Hobbs PCD, Abraham DW, Wickramasinghe HK (1989) Magnetic force microscopy with 25 nm resolution. Appl. Phys. Lett. **55**, 2357-2359.

Husser OE, Craston DH, Bard AJ (1989) Scanning electrochemical microscopy: High resolution deposition and etching of metals. J. Electrochem. Soc. **136**, 3222-3229.

Ibe JP, Bey Jr. PP, Brandow SL, Brizzolara RA, Burnham NA, DiLella DP, Lee KP, Marrian CRK, Colton RJ (1990) On the electrochemical etching of tips for scanning tunneling microscopy. J. Vac. Sci. Technol. **A 8**, 3570-3575.

Israelachvili JN (1985) *Intermolecular and surface forces: with applications to colloidal and biological systems*. Academic Press, Orlando, 137-140.

Jahanmir J (1988) Application of the scanning tunneling microscope to the lithographic microprocessing of silicon in air. Ph.D. Dissertation, Cornell University, Ithaca, New York.

Kaiser WJ, Bell LD (1988) Direct observation of subsurface interface electronic structure by ballistic electron-emission spectroscopy. Phys. Rev. Lett. **60**, 1406-1409.

Kaiser WJ, Bell LD, Hecht MH, Grunthaner FJ (1988) Scanning tunneling microscopy characterization of the geometric and electronic structure of hydrogen-terminated silicon surfaces. J. Vac. Sci. Technol. A **6**, 519-523.

Kaiser WJ, Jaklevic RC (1986) Spectroscopy of electronic states of metals with a STM. IBM J. Res. Develop. **30**, 411-416.

Kaizuka H, Siu B (1988) A simple way to reduce hysteresis and creep when using piezoelectric actuators. Jpn. J. Appl. Phys. **27**, L773-L776.

Keller D, Bustamante C, Leller RW (1989) Imaging of single uncoated DNA molecules by scanning tunneling microscopy. Proc. Natl. Acad. Sci. **86**, 5356-5360.

Kwak J, Bard AJ (1989) Scanning electrochemical microscopy. Apparatus and two-dimensional scans of conductive and insulating substrates. Anal. Chem. **61**, 1794-1799.

Kwak J, Lee C, Bard AJ (1990) Scanning electrochemical microscopy: A study of the conductivity of a polypyrrole film. J. Electrochem. Soc. **137**, 1481-1484.

Landman U, Luedtke WD, Burnham NA, Colton RJ (1990) Atomistic mechanisms and dynamics of adhesion, nanoindentation, and fracture. Science **248**, 454-461.

Lee G, Arscott PG, Bloomfield VA, Evans DF (1989) Scanning tunneling microscopy of nucleic acids. Science **244**, 475-477.

Lennard-Jones JE (1932) Processes of adsorption and diffusion on solid particles. Trans. Faraday Soc. **28**, 333-359.

Lev O, Fan F, Bard AJ (1988) The application of scanning tunneling microscopy to *in situ* studies of nickel electrodes under potential control. J. Electrochem Soc. **135**, 783-784.

Li M-Q, Zhu J-D, Zhu J-Q, Hu J, Gu M-M, Xu Y-L, Zhang L-P, Huang Z-Q, Xu L-Z, Yao Z-W (1991) Direct observation of B-form and Z-form DNA by scanning tunneling microscopy. J. Vac. Sci. Technol. **B 9**, 1298-1303.

Lin CW, Fan F, Bard AJ (1987) High resolution photoelectrochemical etching of n-GaAs with the scanning electrochemical and tunneling microscope. J. Electrochem. Soc. **134**, 1038-1039.

Lindsay SM (1989) Imaging biological polymers in water. EMSA Bulletin **19**, 60-64.

Lindsay SM, Li Y, Pan J, Thundat T, Nagahara LA, Oden P, DeRose JA, Knipping U (1991) Studies of the electrical properties of large molecular adsorbates. J. Vac. Sci. Technol. **B 9**, 1096-1101.

Lindsay SM, Nagahara LA, Thundat T, Knipping U, Rill RL, Drake B, Prater CB, Weisenhorn AL, Gould SAC, Hansma PK (1989b) STM and AFM images of nucleosome DNA under water. J. Biomol. Struct. Dyn. **7**, 279-287.

Lindsay SM, Nagahara LA, Thundat T, Oden P (1989c) Sequence, packing and nanometer scale structure in STM images of nucleic acids under water. J. Biomol. Struct. Dyn. **7**, 289-299.

Lindsay SM, Sankey OF, Li Y, Herbst C, Rupprechet A (1990) Pressure and resonance effects in scanning tunneling microscopy of molecular adsorbates. J. Phys. Chem. **94**, 4655-4660.

Lindsay SM, Thundat T, Nagahara L (1988) Adsorbate deformation as a contrast mechanism in STM images of biopolymers in an aqueous environment: Images of the unstained, hydrated DNA double helix. J. Microscopy **152**, 213-219.

Lindsay SM, Thundat T, Nagahara L, Knipping U, Rill RL (1989a) Images of the DNA double helix in water. Science **244**, 1063-1064.

Lyding JW, Skala S, Jubacek JS, Brockenbrough R, Gammie G (1988) Design and operation of variable temperature STM. J. Microscopy **152**, 371-378.

Mainsbridge B, Thundat T (1991) Scanning tunneling microscopy of chloroplasts. J. Vac. Sci. Technol. **B 9**, 1259-1262.

Mamin HJ, Chiang S, Birk H, Guethner PH, Rugar D (1991) Gold deposition from a scanning tunneling microscope tip. J. Vac. Sci. Technol. **B 9**, 1398-1402.

Mamin HJ, Ganz E, Thomson RE, Clarke J (1986) Contamination-mediated deformation of graphite by the scanning tunneling microscope. Phys. Rev. **B 34**, 9015-9018.

Mamin HJ, Guethner PH, Rugar D (1990) Atomic emission from a gold scanning-tunneling-microscope tip. Phys. Rev. Lett. **65**, 2418-2421.

Mandler D, Bard AJ (1990) High resolution etching of semiconductors by the feedback mode of the scanning electrochemical microscope. J. Electrochem. Soc. **137**, 1468-2472.

Marchon B, Bernhardt P, Bussell ME, Somorjai SE, Salmeron M, Sickhaus W (1988) Atomic arrangement of sulfur adatoms on Mo(001) at atmospheric pressure: A scanning tunneling microscopy study. Phys Rev. Lett. **60**, 1166-1169.

Marrian CRK, Dobisz EA (1991) Investigation of undeveloped e-beam resist with a scanning tunneling microscope. J. Vac. Sci. Technol. **B 9**, 1367-1370.

Marrian CRK, Dobisz EA, Colton RJ (1990) Lithographic studies of an e-beam resist in a vacuum scanning tunneling microscope. J. Vac. Sci. Technol. **A 8**, 3563-3569.

Martin Y, Williams CC, Wickramasinghe HK (1987) Atomic force microscope-force mapping and profiling on a sub 100-Å scale. J. Appl. Phys. **61**, 4723-4729.

Masai J, Shibata T, Kondo S, Ishiwata S (1991) Scanning tunneling microscopy of actin filament. J. Vac. Sci. Technol. **B 9**, 1177-1179.

Mate CM, Lorenz MR, Novotny VJ (1989) Atomic force microscopy of polymeric liquid films. J. Chem. Phys. **90**, 7550-7555.

Mate CM, McClelland GM, Erlandsson R, Chiang S (1987) Atomic-scale friction of a tungsten tip on a graphite surface. Phys. Rev. Lett. **59**, 1942-1945.

McClelland GM, Erlandsson R, Chiang S (1987) Atomic force microscopy: General principles and a new implementation. In: *Reviews of Progress in Quantitative Non-Destructive Evaluation*, Thompson DO, Chimenti DE (eds.), Plenum Press, New York Vol. **6B**, 1307.

McCord MA, Kern DP, Chang THP (1988) Direct deposition of 10-nm metallic features with the scanning tunneling microscope. J. Vac. Sci. Technol. **B 6**, 1877-1880.

McCord MA, Pease RFW (1987a) Scanning tunneling microscope as a micromechanical tool. Appl. Phys. Lett. **50**, 569-570.

McCord MA, Pease RFW (1987b) Exposure of calcium fluoride resist with the scanning tunneling microscope. J. Vac. Sci. Technol. **B 5**, 430-433.

McCord MA, Pease RFW (1986) Lithography with STM. J. Vac. Sci. Technol. **B 4**, 86-88.

McCord MA, Pease RFW (1988) Lift-off metallization using poly(methyl methacrylate) exposed with a scanning tunneling microscope. J. Vac. Sci. Technol. **B 6**, 293-296.

Melmed AJ (1991) The art and science and other aspects of making sharp tips. J. Vac. Sci. Technol. **B 9**, 601-608.

Meyer G, Amer NM (1988) Novel optical approach to atomic force microscopy, Appl. Phys. Lett. **53**, 1045-1047.

Meyer G, Amer NM (1990) Optical-beam-deflection atomic force microscopy: The NaCl(001) surface. Appl. Phys. Lett. **56**, 2100-2101.

Meyer E, Wiesendanger R, Anselmetti D, Hidber HR, Güntherodt H-J, Levy F, Berger H (1990) Different response of atomic force microscopy and scanning tunneling microscopy to charge density waves. J. Vac. Sci. Technol. **A 8**, 495-499.

Meyer, E, Heinzelmann H, Brodbeck D, Overney R, Howald L, Hug H, Jung T, Hidber H-R, Güntherodt H-J (1991) Atomic resolution in the surface of LiF (100) by atomic force microscopy. J. Vac. Sci. Technol. **B 9**, 1329-1332.

Meyer E, Heinzelmann H, Rudin H, Güntherodt H-J (1989) Atomic resolution in LiF (001) by atomic force microscopy. Z. Phys. **B 79**, 3-4.

Miyamoto T, Kaneko R (1991) Tribological characteristics of amorphous carbon films investigated by point contact microscopy. J. Vac. Sci. Technol. **B 9**, 1336-1339.

Miyamoto T, Kaneko R, Ando Y (1990) Interaction force between thin film disk media and elastic solids investigated by atomic force microscopy. J. Tribol. Trans. ASME **112**, 567-572.

Mizes HA, Park S, Harrison WA (1987) Multiple-tip interpretation of anomalous scanning-tunneling-microscopy images of layered materials. Phys. Rev. **B 36**, 4491-4494.

Musselman IH, Russell PE (1990) Platinum/iridium tips with controlled geometry for scanning tunneling microscopy. J. Vac. Sci. Technol. **A 8**, 3558-3562.

Nagahara LA, Thundat T, Lindsay SM (1989) Preparation and characterization of STM tips for electrochemical studies. Rev. Sci. Instrum. **60**, 3128-3130.

Nagahara LA, Thundat T, Lindsay SM (1990) Nanolithography on semiconductor surfaces under an etching solution. Appl. Phys. Lett. **57**, 270-272.

Neddermeyer H (1990) STM studies of nucleation and the initial stages of film growth. Critical Reviews in Solid State and Materials Sciences **16**, 309-335.

Newcomb CV, Flinn I (1982) Improving the linearity of piezoelectric ceramic actuators. Electron. Lett. **18**, 442-444.

Nishikawa O, Hattori K, Katsuki F, Tomitori M (1988) Field ion microscope and atom probe studies of STM tips. J. Phys. Colloque **49**, 55-59.

Nogami J, Baski AA, Quate CF (1990) Behavior of gallium on vicinal Si(100) surfaces. J. Vac. Sci. Technol. **A 8**, 3520-3523.

Penner RM, Heben MJ, Lewis NS (1989) Preparation and electrochemical characterization of conical and hemispherical ultramicroelectrodes. Anal. Chem. **61**, 1630-1636.

Pohl DW (1986) Some design criteria in STM. IBM J. Res. Develop. **30**, 417-427.

Pohl DW (1987) Sawtooth nanometer slider: a versatile low voltage piezoelectric translation device. Surf. Sci. **181**, 174-175.

Pohl DW, Denk W, Lanz M (1988) Optical stethoscopy: Image recording with resolution $\lambda/20$. Appl. Phys. Lett. **44**, 651-653.

Quate CF (1986) Vacuum tunneling: A new technique for microscopy. Phys. Today **39**, 26-33.

Reddick RC, Warmack RJ, Ferrell TL (1989) New form of scanning optical microscopy. Phys. Rev. **B 39**, 767-770.

Reiss G, Schneider F, Vancea J, Hoffmann H (1990) Scanning tunneling microscopy on rough surfaces: Deconvolution of constant current images. Appl. Phys. Lett. **57**, 867-869.

Ringger M, Corb BW, Hidber H-R, Schlogl R, Wiesendanger R, Stemmer A, Rosenthaler L, Brunner AJ, Oelhafen PC, Gunterodt H-J (1986) STM activity at University of Basel. IBM J. Res. Develop. **30**, 500-507.

Robinson RS (1988) Real-time scanning tunneling microscopy of surfaces under active electrochemical control. J. Microscopy **152**, 541-546.

Rugar D, Mamin HJ, Erlandsson R, Stern JE,Terris BD (1988) Force microscope using a fiber-optic displacement sensor. Rev. Sci. Instrum. **59**, 2337-2340.

Rugar D, Mamin HJ, Guethner PH, Lambert SE, Stern JE, McFadyen I, Yogi T (1990) Magnetic force microscopy: General principles and application to longitudinal recording media. J. Appl. Phys. **68**, 1169-1183.

Salmeron M, Beebe T, Odriozola J, Wilson T, Ogletree DF, Siekhaus W (1990) Imaging biomolecules with the scanning tunneling microscope: problems and prospects. J. Vac. Sci. Technol. **A 8**, 635-641.

Sarid D (1991) *Scanning Force Microscopy with Applications to Electric, Magnetic, and Atomic Forces*. Oxford University, New York.

Sarid D, Iams DA, Ingle JT, Weissenberger V, Ploetz J (1990) Performance of a scanning force microscope using a laser diode. J. Vac. Sci. Technol. **A 8**, 378-382.

Sarid D, Iams D, Weissenberger V, Bell LS (1988) Compact scanning-force microscope using a laser diode. Optics Lett. **13**, 1057-1059.

Schneir J, Hansma PK, Elings V, Gurley J, Wickramasinghe K, Sonnenfeld R (1988b) Creating and observing surface features with a scanning tunneling microscope. Proc. SPIE **897**, 16-19.

Schneir J, Sonnenfeld R, Hansma PK,Tersoff J (1986) Tunneling microscopy study of the graphite surface in air and water. Phys. Rev. **B 34**, 4979-4984.

Schneir J, Sonnenfeld R, Marti O, Hansma PK, Demuth JE, Hamers RJ (1988a) Tunneling microscopy, lithography, and surface diffusion on an easily prepared, atomically flat gold surface. J. Appl. Phys. **63**, 717-721.

Shih CK, Feenstra RM, Maartensson P (1990) Scanning tunneling microscopy and spectroscopy of thin metal films on the gallium arsenide(110) surface. J. Vac. Sci. Technol. **A 8**, 3379-3385.

Sonnenfeld R, Hansma PK (1986) Atomic-resolution microscopy in water. Science **232**, 211-213.

Staufer U, Scandella L, Rudin H, Güntherodt H-J, Garcia N (1991) Tailoring nanostructures with a scanning tunneling microscope. J. Vac. Sci. Technol. B **9**, 1389-1393.

Staufer U, Wiesendanger R, Eng L, Rosenthaler L, Hidber HR, Günterodt H-J, Garcia N (1987) Nanometer scale structure fabrication with the STM. Appl. Phys. Lett. **51**, 244-246.

Stoll E (1984) Resolution of the scanning tunnel microscope. Surf. Sci. **143**, L411-L416.

Strecker H, Persch G (1991) Application of scanning tunneling microscope in magnetic storage device manufacturing. J. Vac. Sci. Technol. **B 9**, 663-665.

Stroscio JA, Feenstra RM, Fein AP (1987) Local state density and long range screening of adsorbed oxygen atoms on the GaAs(110) surface. Phys. Rev. Lett. **58**, 1668-1671.

Terris BD, Stern JE, Rugar D, Mamin HJ (1990) Localized charge force microscopy. J. Vac. Sci. Technol. **A 8**, 374-377.

Tersoff J, Hamann DR (1983) Theory and application for the scanning tunneling microscope. Phys. Rev. Lett. **50**, 1998-2001.

Thompson WT (1987) Vibrations. In: *Marks' Standard Handbook for Mechanical Engineers*, Avallone EA, Baumeister III T (eds.), McGraw-Hill Book Company, New York, Chapter 5, 74-75.

Tortonese M, Yamada H, Barrett RC, Quate CF (1991) Atomic force microscopy using a piezoresistive cantilever. Proceedings of International Conference on Solid-State Sensors and Actuators, 448-451.

Trevor DJ, Chidsey CED, Loiacono DN (1989) *In situ* scanning-tunneling-microscope observation of roughening, annealing, and dissolution of Gold(111) in an electrochemical cell. Phys. Rev. Lett. **62**, 929-932.

van de Leemput LEC, Rongen PHH, Timmerman BH, van Kempen H (1991) Calibration and characterization of piezoelectric elements as used in scanning tunneling microscopy. Rev. Sci. Instrum. **62**, 989-992.

van Kempen H, van de Walle GFA (1986) Applications of a high-stability STM. IBM J. Res. Develop. **30**, 509-514.

Vasile MJ, Grigg DA, Griffith JE, Fitzgerald EA, Russell PE (1991) Scanning probe tips formed by focused ion beams. Rev. Sci. Instrum. **62**, 2167-2171.

Vedosic JP (1987) Mechanics of Materials. In: *Marks' Standard Handbook for Mechanical Engineers*, Avallone EA and Baumeister III T (eds.), McGraw-Hill Book Company, New York, Chapter 5, 23.

Weisenhorn AL, Drake B, Prater CB, Gould SAC, Hansma PK, Ohnesorge F, Egger M, Heyn S-P, Gaub HE (1990) Immobilized proteins in buffer solution imaged at molecular resolution by atomic force microscopy. Biophys. J. **58**, 1251-1258.

Weisenhorn AL, Egger M, Ohnesorge F, Gould SAC, Heyn S-P, Hansma HG, Sinsheimer RL, Gaub HE, Hansma PK (1991) Molecular-resolution images of Langmuir-Blodgett films and DNA by atomic force microscopy. Langmuir **7**, 8-12.

Weisenhorn AL, MacDougall JE, Gould SAC, Cox SD, Wise WS, Massie J, Maivald P, Elings VB, Stucky GD, Hansma PK (1990) Imaging and manipulating molecules on zeolite surface with an atomic force microscope. Science **247**, 1330-1333.

Welland ME, Miles MJ, Lambert N, Morris VJ, Coombs JH, Pethica JB (1989) Structure of the globular protein vicilin revealed by scanning tunneling microscopy. Int. J. Biol. Macromol. **11**, 29-32.

Wiechers J, Twomey T, Kolb DM, Behm RJ (1988) An *in situ* STM study of Au(111) with atomic scale resolution. J. Electroanal. Chem. **248**, 451-460.

Williams CC, Slinkman J, Hough WP, Wickramasinghe HK (1990) Lateral dopant profiling on a 100 nm scale by scanning capacitance microscopy. J. Vac. Sci. Technol. **A 8**, 895-898.

Williams CC, Wickramasinghe HK (1986) Scanning thermal profiler. Appl. Phys. Lett. **49**, 1587-1589.

Wolter O, Bayer Th, Greschner J (1991) Micromachined silicon sensors for scanning force microscopy. J. Vac. Sci. Technol. **B 9**, 1353-1357.

Wu S, Ng K-W (1991) A piezoelectric-driven micropositioner with magnetic locking mechanism. Rev. Sci. Instrum. **62**, 93-95.

Yamada H, Fujii T, Nakayama K (1989) Linewidth measurement by a new STM. Jpn. J. Appl. Phys. **28**, 2402-2404.

Young R, Ward J, Scire HF (1972) The topografiner: An instrument for measuring surface microtopography. Rev. Sci. Instrum. **43**, 999-1011.

Youngquist MG, Driscoll RJ, Coley TR, Goddard WA, Baldeschwieler JD (1991) Scanning tunneling microscopy of DNA: Atom-resolved imaging, general observations and possible contrast mechanism. J. Vac. Sci. Technol. **B 9**, 1304-1308.

Yuan J-Y, Shao Z (1990) Simple model of image formation by scanning tunneling microscopy of nonconducting materials. Ultramicroscopy **34**, 223-226.

Editor's Note: All of the reviewer's concerns were appropriately addressed by text changes, hence there is no Discussion with Reviewers.